BRNO UNIVERSITY OF TECHNOLOGY
VYSOKÉ UČENÍ TECHNICKÉ V BRNĚ

FACULTY OF MECHANICAL ENGINEERING
FAKULTA STROJNÍHO INŽENÝRSTVÍ

INSTITUTE OF PHYSICAL ENGINEERING
ÚSTAV FYZIKÁLNÍHO INŽENÝRSTVÍ

THEORETICAL STUDY OF MAGNETIC ANISOTROPY IN MGO-BASED MAGNETIC TUNNEL JUNCTIONS

TEORETICKÁ STUDIE MAGNETICKÉ ANIZOTROPIE V MAGNETICKÝCH TUNELOVÝCH SPOJÍCH NA BÁZI MGO

MASTER'S THESIS
DIPLOMOVÁ PRÁCE

AUTHOR — **Bc. Libor Vojáček**
AUTOR PRÁCE

SUPERVISOR — **Prof. Mairbek Chshiev, Ph.D.**
VEDOUCÍ PRÁCE

BRNO 2021

BRNO UNIVERSITY OF TECHNOLOGY
FACULTY OF MECHANICAL ENGINEERING

Assignment Master's Thesis

Institut:	Institute of Physical Engineering
Student:	**Bc. Libor Vojáček**
Degree programm:	Physical Engineering and Nanotechnology
Branch:	no specialisation
Supervisor:	**prof. Mairbek Chshiev, Ph.D.**
Academic year:	2020/21

As provided for by the Act No. 111/98 Coll. on higher education institutions and the BUT Study and Examination Regulations, the director of the Institute hereby assigns the following topic of Master's Thesis:

Theoretical Study of Magnetic Anisotropy in MgO–based Magnetic Tunnel Junctions

Brief Description:

A magnetic tunnel junction (MTJ) is a spintronic device commercially used in highly sensitive hard–disk drive reading heads. Since 2007 it has helped to sustain the exponential increase in the magnetic storage density. Moreover, it also became the building block of the fast, durable, power–efficient, and non–volatile magnetic random–access memory (MRAM). Just like reading heads, this new type of solid–state memory uses MTJs based on crystalline magnesium oxide (MgO) along with 3d metallic magnetic elements (Fe and Co). Strong magnetic anisotropy in the direction perpendicular to the metal|MgO interface is needed to provide long–term thermal memory stability as the device is downscaled. This work will analyze the magnetocrystalline anisotropy (MCA) of body–centered cubic Fe, Co, and Ni on MgO using ab initio simulations. Numerical code will be developed to calculate the shape anisotropy, crucial to consider in addition to MCA, because together they add up to the effective anisotropy. Finally, a calculation of MCA based on the second–order perturbation theory will be implemented. This will enable us to link the observed anisotropic properties directly to the system's electronic structure (the band structure and density of states).

Master's Thesis goals:

1. Review the state–of–the–art on the topics of density functional theory (DFT) and magnetic anisotropy.
2. Calculate the magnetocrystalline anisotropy in thin layers of body–centered cubic Fe, Co, and Ni on MgO using the Vienna Ab initio Simulation Package (VASP). Develop code for calculations of shape anisotropy in these structures.
3. Develop code to calculate magnetocrystalline anisotropy directly from the electronic structure in the framework of second–order perturbation theory.

Recommended bibliography:

DIENY, B. a M. CHSHIEV. Perpendicular magnetic anisotropy at transition metal/oxide interfaces and applications. Reviews of Modern Physics. 2017, 89(2). ISSN 0034-6861.

MARTIN, R. M. Electronic Structure: Basic Theory and Practical Methods, 2nd ed. Cambridge University Press, 2020. ISBN 978-1108429900

BRUNO, P. Physical Origins and Theoretical Models of Magnetic Anisotropy. Ferienkurse Des Forschungszentrums Julich, 1993.

Deadline for submission Master's Thesis is given by the Schedule of the Academic year 2020/21

In Brno,

L. S.

prof. RNDr. Tomáš Šikola, CSc. Director of the Institute	doc. Ing. Jaroslav Katolický, Ph.D. FME dean

Summary
A magnetic tunnel junction (MTJ) is a spintronic device commercially used in highly sensitive hard disk drive reading heads. Since 2007 it has helped to sustain the exponential increase in the magnetic storage density. Moreover, it also became the building block of the fast, durable, power-efficient, and non-volatile magnetic random-access memory (MRAM). Just like reading heads, this new type of solid-state memory uses MTJs based on crystalline magnesium oxide (MgO) along with 3d metallic magnetic elements (Fe and Co). Strong magnetic anisotropy in the direction perpendicular to the metal|MgO interface is needed to provide long-term thermal memory stability as the device is downscaled. This work will analyze the magnetocrystalline anisotropy (MCA) of body-centered cubic Fe, Co, and Ni on MgO using ab initio simulations. Numerical code will be developed to calculate the shape anisotropy, crucial to consider in addition to MCA because together they add up to the effective anisotropy. Finally, a calculation of MCA based on the second-order perturbation theory will be implemented. This will enable us to link the observed anisotropic properties directly to the system's electronic structure (the band structure and density of states).

Abstrakt
Magnetický tunelový spoj (MTJ) je spintronická součástka komerčně používaná ve vysoce citlivých čtecích hlavách pevných disků. Počínaje rokem 2007 přispěla k udržení exponenciálního nárůstu hustoty magnetického zápisu. Kromě toho se také stala stavebním kamenem rychlé, odolné, úsporné a nevolatilní magnetické paměti s přímým přístupem (MRAM). Tento nový typ polovodičové paměti, stejně jako je tomu u čtecích hlav disků, využívá tunelové spoje založené na krystalickém oxidu hořečnatém (MgO) spolu s 3d kovovými magnetickými prvky (Fe a Co). Pro zmenšení MTJ a současné udržení dlouhodobé stability paměti proti tepelným fluktuacím je zapotřebí silná magnetická anizotropie ve směru kolmém na rozhraní kov|MgO. V této práci proto nejdříve provedeme analýzu magnetokrystalické anizotropie (MCA) kubického prostorově centrovaného Fe, Co a Ni na MgO pomocí ab initio simulací. Dále bude vyvinut program pro výpočet tvarové anizotropie, která je kromě MCA velmi podstatná, neboť v součtu dávají efektivní anizotropii. Na závěr implementujeme program pro výpočet MCA na základě poruchové teorie druhého řádu. To nám umožní dát pozorované anizotropní vlastnosti do souvislosti přímo s elektronickou strukturou systému (pásovou strukturou a hustotou stavů).

Keywords
perpendicular magnetic anisotropy, enhancement, bcc Co, MgO-based magnetic tunnel junctions, MTJ, STT-MRAM, downscaling, thin films, spintronics

Klíčová slova
kolmá magnetická anizotropie, zlepšení, bcc Co, magnetické tunelové spoje na bázi MgO, MTJ, STT-MRAM, downscaling, tenké vrstvy, spintronika

VOJÁČEK, Libor. *Theoretical Study of Magnetic Anisotropy in MgO-based Magnetic Tunnel Junctions*. Brno, 2021. 63 p. Master's thesis. Brno University of Technology. Faculty of Mechanical Engineering. Supervised by Mairbek CHSHIEV.

I hereby declare that I have written the present thesis *Theoretical Study of Magnetic Anisotropy in MgO-based Magnetic Tunnel Junctions* independently, without assistance from external parties, and without the use of other resources than those indicated. The ideas taken directly or indirectly from external sources (including electronic sources) are duly acknowledged in the text. The material, either in full or in part, has not been previously submitted for grading at this or any other academic institution.

Bc. Libor Vojáček

My sincere gratitude goes to Prof. Mairbek Chshiev, who introduced me to the world of ab initio modeling and diligently supervised my work during my Erasmus internship and beyond. I want to thank Dr. Fatima Ibrahim, who helped me solve many technical issues and contributed with important ideas during our discussions. I am indebted to Dr. Bernard Dieny for his many important insights and overview. I am thankful to Dr. Ali Hallal for very stimulating conversations. My sincere appreciation to all the fantastic people at SPINTEC whom I had the privilege to meet, work with, laugh with, and hike with.

Děkuji svým rodičům, kteří mě ustavičně motivovali a podporovali ve studiu.

Děkuji Dr. Vojtěchu Uhlířovi, který mou stáž inicioval a spolu s Dr. Jonim Arregim byli od začátku mými moudrými průvodci ve světě magnetismu.

Děkuji svým dobrým kamarádům na Ústavu fyzikálního inženýrství za společně strávené chvíle. Děkuji zejména Ing. Ondřeji Wojewodovi, který text pročetl a přispěl cennými připomínkami.

Bc. Libor Vojáček

Financial support of the Thermo Fisher Scientific scholarship is gratefully acknowledged.

Contents

Introduction **1**

1. Magnetic anisotropy **5**
1.1. Phenomenological expressions . . . 5
1.2. Volume vs. interface anisotropy . . . 6
1.3. Shape, magnetocrystalline, and induced anisotropy . . . 7
1.4. Dipolar interaction effects . . . 7
1.5. Spin-orbit coupling effects . . . 8
1.6. Magnetic anisotropy in data storage . . . 9

2. Density functional theory (DFT) **11**
2.1. Many-body Schrödinger equation . . . 11
2.2. Born-Oppenheimer approximation . . . 12
2.3. Hartree-Fock approximation . . . 13
2.4. Exchange-correlation hole . . . 13
2.5. Thomas-Fermi method . . . 15
2.6. Hohenberg-Kohn theorems . . . 15
2.7. Kohn-Sham equations . . . 17
2.8. Self-consistent cycle . . . 19
2.9. Exchange-correlation functionals . . . 21
2.10. Plane-wave basis and PAW method . . . 22
2.11. Spin-dependent Kohn-Sham equation . . . 24
2.12. Magnetocrystalline anisotropy calculation . . . 25
2.13. Vienna *Ab Initio* Simulation Package (VASP) . . . 25

3. Magnetic anisotropy of bcc Fe, Co, and Ni/MgO ultrathin films **27**
3.1. Magnetocrystalline anisotropy calculation procedure . . . 27
3.2. Convergence tests . . . 28
3.3. Body-centered cubic (bcc) lattice of Co and Ni . . . 29
3.4. Test calculations: reproducing published results . . . 30
3.5. Varying the metal thickness . . . 31
3.6. Strained bulk bcc Fe, Co, and Ni . . . 33

4. Giant anisotropy enhancement in Fe/Co/Fe|MgO magnetic tunnel junction **35**
4.1. PMA enhancement due to E_{MCA} . . . 35
4.2. Shape anisotropy (E_{dd}) calculation . . . 36
4.3. PMA enhancement due to E_{MCA} and E_{dd} . . . 38

4.4. Decrease of PMA with Fe/Co interdiffusion 39
4.5. Fabrication of the metastable bcc Co 40
4.6. Tunneling magnetoresistance 40

5. Second order perturbation theory calculations of E_{MCA} 43
5.1. Bruno's theory 43
5.2. Density of states (DOS)-based E_{MCA} calculation 43
5.3. Band structure-based E_{MCA} calculation 47

Conclusion 49

References 51

List of abbreviations 63

A. Supporting ab initio results i

Introduction

A spintronic device called the *magnetic tunnel junction* (MTJ) [1, 2] consists of two magnetic layers separated by an insulating barrier [Fig. 1(a)]. It exhibits the *tunneling magnetoresistance* effect (TMR) [3, 4], which means there is a large change of resistance when one of the magnetic layers is switched. MTJs are used for several cutting edge applications [5, 6]: reading heads in hard disk drives (HDDs) [7], memory bits in the magnetoresistive random-access memory (MRAM) [8], and highly sensitive magnetic sensors. Besides, there are emerging applications of MTJs as artificial neurons [9], random number generators [10], microwave generators [11], and processing elements in stochastic computing [12]. In this introduction, we take a deeper look at the impact of MTJs on data storage.

The famous Moore's law [13], postulated for semiconductor chips, also holds for the most widely used computer storage medium, which is the magnetic hard disk drive (HDD) [14]. The sustained exponential growth of HDD storage density in the past decades is clear from Fig. 1(c).

Increasing the storage density required shrinking and improving the essential components [Fig. 1(b)], and the success of HDDs would not be possible without developing more sensitive reading heads. The latest generation of reading heads is based on MTJs, where the magnetization orientation of the upper layer is usually fixed [Fig. 1(a)]. In contrast, the bottom layer is free to rotate and respond to the magnetic information written on the platter below. Note that the tunnel barrier in an MTJ is usually made of crystalline magnesium oxide (MgO) because of its high TMR [15–17]. We are then talking about MgO-based MTJs.

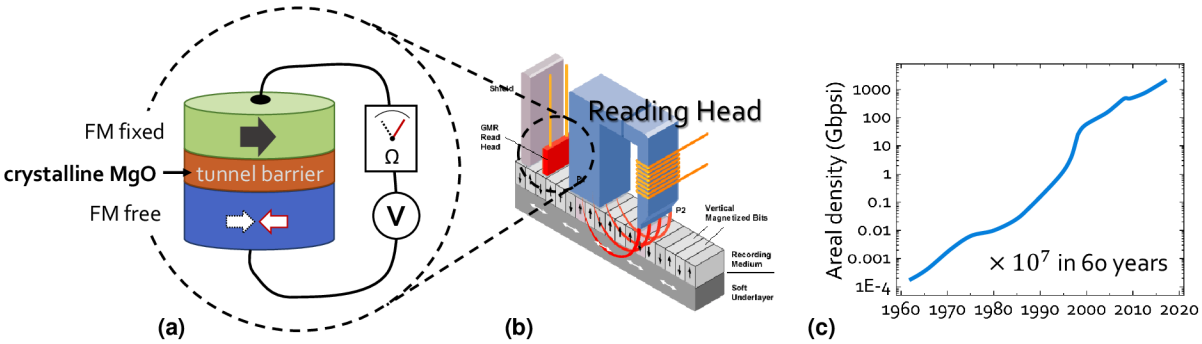

Figure 1: (a) A magnetic tunnel junction used in the latest reading heads. It consists of two ferromagnetic (FM) layers separated by a tunnel barrier. In MTJs serving as reading heads, the magnetization lies horizontally (along the film plane), as shown in the figure. (b) The main components of an HDD [18]. The reading head is of our main interest. (c) Moore's law for HDDs, demonstrating a seven-order increase of their storage density in the past 60 years. After [19].

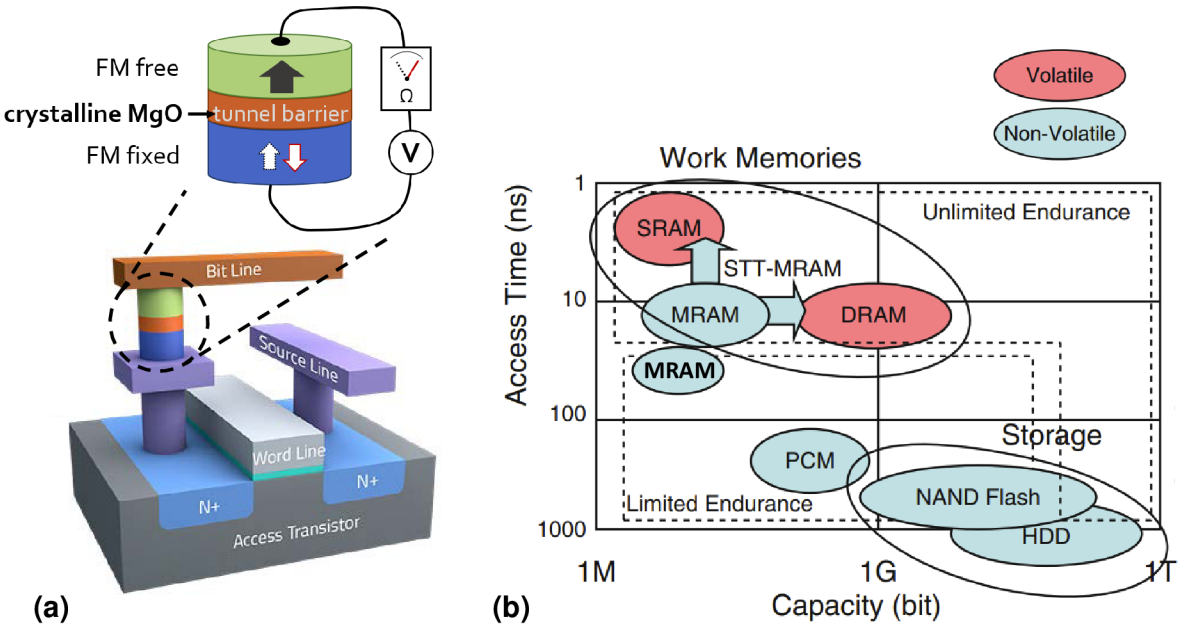

Figure 2: (a) MTJs can also be used as memory bits in the MRAM memory. Here, the magnetization is perpendicular to the film plane. After [20]. (b) Compared to other types of memories, MRAM is fast and non-volatile, with moderate capacity, but very large endurance. Hence, it is well suited to replace SRAM and DRAM memories as the work memory in certain hierarchy levels displayed in Fig. 3. From [21].

MgO-based MTJ has another important application, besides reading the digital information in HDDs: it can be used as a memory bit, to *store* the information as well. It can store the binary information in its free ferromagnetic layer and then read it out by the TMR effect. They form the aforementioned *magnetoresistive random access memory* (MRAM), sketched in Fig. 2(a). In Fig. 2(b), MRAM is placed in context and compared with other types of memories. Because it is fast, it is well suited as the *work memory*. We should make a clear distinction between the *storage memory* and the work memory.

Storage memory is meant to preserve data in the long term. HDDs are used as storage memory because they are cheap and have large data capacity, but they are also quite slow [Fig. 2(b)]. An alternative to HDDs is the (NAND) Flash memory, widely used in USB flash drives and solid-state drives (SSD). It is a few times faster and also more reliable than HDDs because it does not contain moving parts. The trade-off is its higher price. Also, the endurance of Flash memory is quite limited[1] [22] and its low speed does not allow for its use as the work memory [Fig. 2(b)].

Work memory holds data that is actively processed by the central processing unit (CPU). *Processor registers* are the fastest and therefore located directly inside the CPU [Fig. 3(a)]. One level lower in the memory hierarchy, we find the processor *cache*, usually represented by the *static random-access memory* (SRAM). Each bit in SRAM consists of several transistors connected into a *latch (flip-flop) circuit* [23]. One level below, there is the much slower *main memory*, usually represented by dynamic random-access memory (DRAM). In DRAM, the bit is composed of one transistor and one capacitor. The capaci-

[1] to about 10^5 write cycles/bit

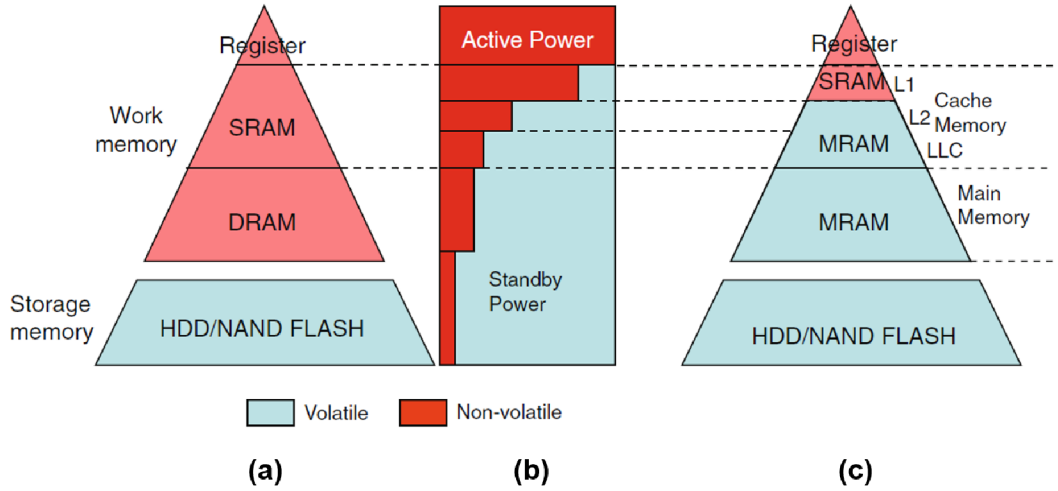

Figure 3: (a) The usual memory hierarchy. Higher level means faster, closer to the CPU, but also lower data capacity. (b) Power dissipated in active and standby mode for the different memory levels. (c) A new hierarchy scheme for lower power dissipation. The (non-volatile) MRAM is introduced as a work memory in levels where the standby power consumption plays an important role. From [21].

tor is either charged or discharged, representing a one or a zero. Both SRAM and DRAM require an external power source even in standby mode; otherwise, the data is lost: they are *volatile memories*.

Both the lower-level cache and the main memory spend a lot of power on maintaining its standby mode, as shown in Fig. 3(b) [21]. Therefore, replacing these memories with a non-volatile memory such as MRAM [Fig. 3(c)], where the written information is permanent and does not need to be maintained by an external power source, can considerably reduce the energy consumption of electronics [21].

In 2018, a new generation of MRAM, the spin-transfer torque MRAM (STT-MRAM), entered volume production [24]. In STT-MRAM, the effect of spin-transfer torque (STT) is exploited: the magnetization of the free layer is switched by a spin-polarized electric current. The current becomes spin-polarized by first passing through the fixed magnetic layer [25, 26]. It is required that the MTJs used as memory bits in STT-MRAM have (1) high tunneling magnetoresistance for good information read-out, (2) high spin-transfer torque efficiency for good information writing, and (3) high magnetic anisotropy for good thermal stability and therefore, memory retention [1, 27]. All these requirements are satisfied in perpendicularly magnetized MgO-based MTJs with the ferromagnetic layers composed of Fe and Co [28], which are therefore the main interest of this work.

In this work, we focus on increasing the perpendicular magnetic anisotropy (PMA) of MgO-based magnetic tunnel junctions with bcc Fe, Co, and Ni as the free magnetic layer. By increasing PMA, the STT-MRAM memory bits can be made smaller[2], while retaining the same data stability against thermal fluctuations, as discussed in Sec. 1.6.

[2]possibly below 25 nm diameter

The text is organized as follows. In Chapter 1, we introduce the importance of magnetic anisotropy for data storage, the anisotropy types, and physical origins. In Chapter 2, we review the fundamentals of the *density functional theory* (DFT). This computational method is the main tool used in this thesis. Chapter 3 presents our systematic calculations of the magnetic anisotropy in body-centered cubic Fe(Co,Ni)/MgO thin magnetic films. Exploiting the knowledge obtained, in Chapter 4 we propose a magnetic tunnel junction with largely enhanced perpendicular magnetic anisotropy. As already mentioned, increasing the PMA is crucial for the downsize-scaling of STT-MRAM memory bits. Finally, in Chapter 5, we analyze the magnetic anisotropy of strained body-centered cubic (bcc) cobalt in the framework of the second-order perturbation theory.

1. Magnetic anisotropy

In ferromagnetic materials, there is a spontaneous magnetization due to exchange interaction [29–31]. Generally, the direction of this magnetization is not arbitrary, and there are preferential axes with respect to the crystalline structure and shape of the magnetic body. This property is called *magnetic anisotropy*. There is a related quantity called *magnetic anisotropy energy* E_{MA}, which is the energy needed to turn the magnetization from its preferential direction (the *easy axis*) to the least preferred direction (*hard axis*). The energy is rather small, on the order of 10^{-3} to 10^{-6} eV/atom, but it is important, as it corresponds to magnetic fields typically used in experiments [32].

Controlling the magnetic anisotropy is of great importance in technological applications. Large anisotropy is beneficial in permanent magnets and magnetic memories, where the magnetization is required to stay in a specified direction. The physical mechanisms responsible for magnetic anisotropy are of relativistic nature. Its two fundamental origins are the *dipole-dipole interaction* and the *spin-orbit coupling*. However, before discussing the types of magnetic anisotropy and its microscopic mechanisms, we first approach the problem phenomenologically, from symmetry arguments.

1.1. Phenomenological expressions

The E_{MA} is a function of the magnetization direction $\boldsymbol{m} = (m_x, m_y, m_z)$, where $|\boldsymbol{m}| = 1$ (it is a unit vector). Just as any other function, E_{MA} can be expanded in some basis, for instance, in spherical harmonics, or more often in powers of m_x, m_y, and m_z [30, 32]:

$$E_{\mathrm{MA}}(m_x, m_y, m_z) = b_0 + \sum_{i,j\in\{x,y,z\}} b_{ij} m_i m_j + \sum_{i,j,k,l\in\{x,y,z\}} b_{ijkl} m_i m_j m_k m_l + \ldots \tag{1.1}$$

Note that due to time-reversal symmetry, only terms that are even in $\boldsymbol{m}$ are allowed (odd terms are forbidden). The specific symmetry of a given problem usually excludes some additional terms.

In systems suitable for permanent magnets and memory applications, there is a single preferential anisotropy axis (easy axis). We are then talking about the **uniaxial anisotropy**, which is usually well described by a single term from Eq. (1.1); choosing the easy axis along z direction, it is the term $b_{zz}m_z^2$, more often expressed as [30]

$$E_{\mathrm{MA,uniaxial}} = K_1 \sin^2\theta\,, \tag{1.2}$$

where θ is the angle between $\boldsymbol{m}$ and the easy axis, and K_1 is the anisotropy constant (Fig. 1.1). This expression is very important in the context of this work dealing with magnetic thin films, where the uniaxial anisotropy is due to three origins: (a) the shape, (b) interfaces, and (c) strain.

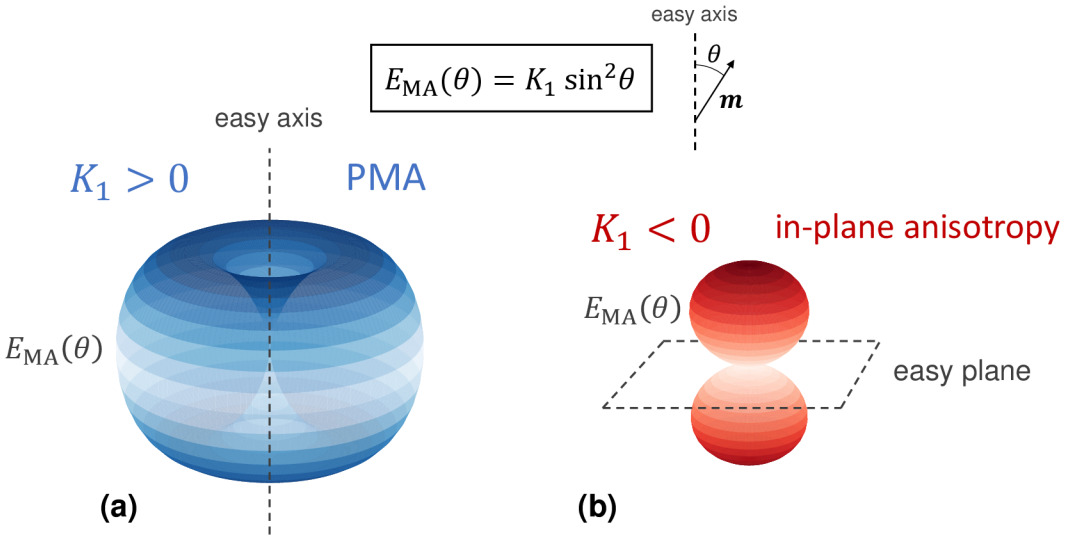

Figure 1.1: The spatial dependence of uniaxial anisotropy energy [Eq. (1.2)] for (a) $K_1 > 0$, signifying the perpendicular anisotropy (PMA), with a single preferential axis for the magnetization called the *easy axis*; and for (b) $K_1 < 0$, signifying an in-plane anisotropy, where the magnetization prefers to lie in any direction along the *easy plane*.

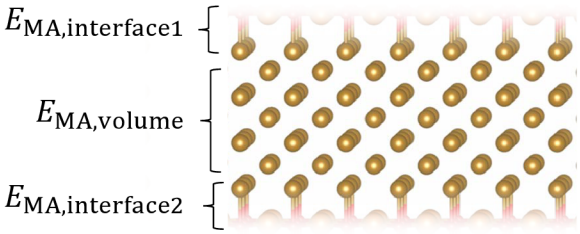

Figure 1.2: A thin magnetic film with the anisotropy coming from the volume and two interfaces [Eq. (1.3)]. Inspired by Dieny and Chshiev [1].

1.2. Volume vs. interface anisotropy

In thin films and nanostructures, the presence of a surface or an interface is a very important factor. An interface induces *interfacial anisotropy*, which is typically much larger than the bulk anisotropy. Because an interface generally breaks the symmetry of a bulk system, it induces uniaxial anisotropy [Eq. (1.2)] in systems, where it would otherwise be forbidden, for instance, in cubic crystals.

The magnetic anisotropy energy can therefore be split into the interface plus volume contribution multiplied by the thin film thickness t

$$E_{\mathrm{MA}} = E_{\mathrm{MA,interface}} + t \cdot E_{\mathrm{MA,volume}} \,, \tag{1.3}$$

see Fig. 1.2. Since we are investigating thin films, the units used here are the units of surface energy, J/m^2, or rather mJ/m^2. For this reason, if there is a constant volume contribution present, E_{MA} should grow linearly with thickness.

1.3. Shape, magnetocrystalline, and induced anisotropy

Based on its origin, magnetic anisotropy may be classified into three categories [30]:

- **Shape anisotropy** is related to the shape of the magnetic body or the magnetic domains in that body. It is of dipolar (magnetostatic) origin [Sec. 1.4]. This magnetostatic energy is minimized when the magnetization lies along the longest side of the magnetic body. In nanowires, the preferential direction is therefore along the wire axis; in (infinite) thin films, it is in any direction in the plane of the film (along the easy plane). In larger magnetic bodies, magnetization breaks into domains, which have their own demagnetizing fields and influence each other by stray fields.

  In the mesoscopic length scales ($\sim$ 100–1000 nm), where the fields from individual atoms are averaged and cannot be resolved, the shape anisotropy follows from the requirement to minimize the demagnetizing energy [30]

  $$E_{\text{demag}} = -\frac{\mu_0}{2} \int_{\Omega} \boldsymbol{H}_{\text{d}} \cdot \boldsymbol{M} \, \mathrm{d}^3 r \,, \tag{1.4}$$

  where the integral is over the magnetic region Ω and the demagnetizing field $\boldsymbol{H}_d$ is related to the magnetization $\boldsymbol{M}$ by

  $$\nabla \cdot \boldsymbol{H}_{\text{d}} = -\nabla \cdot \boldsymbol{M} \,. \tag{1.5}$$

  For infinite thin magnetic films, the shape anisotropy energy is then [30]

  $$E_{\text{demag, thin-film}} = -\frac{1}{2} \mu_0 M_{\text{s}}^2 \,, \tag{1.6}$$

  where μ_0 is the vaccum permeability and M_{s} is the saturation magnetization.

  In this work, however, we deal with length-scales on the order of $\approx$ 0.1 nm and therefore calculate the demagnetizing energy also directly from the dipole-dipole interaction of individual atomic moments [Eq. (1.7)]. The values will be compared with the ones from the simple formula above [Eq. (1.6)] in Sec. 4.2.

- **Magnetocrystalline anisotropy** is intrinsic to the crystal structure. Its main origin is the spin-orbit coupling (SOC) (Sec. 1.4) and partly the dipolar interaction (Sec. 1.5).

- **Induced anisotropy** may appear due to annealing in external magnetic field, or often due to strain [30]. In thin films, the strain is often caused by a lattice mismatch between the epitaxial magnetic layer and the substrate.

1.4. Dipolar interaction effects

In Fe, Co, and Ni, which are $3d$ transition metals, the magnetization of the atoms is distributed almost spherically and can safely be described by the dipolar term, ignoring higher multipoles (quadrupoles, hexapoles, etc.) [32]. The dipole-dipole interaction energy writes [32]

$$E_{\text{dipolar}} = \frac{\mu_B^2}{2} \sum_{i \neq j} \frac{1}{r_{ij}^3} \left(\boldsymbol{m}_i \cdot \boldsymbol{m}_j - 3 \frac{(\boldsymbol{r}_{ij} \cdot \boldsymbol{m}_i)(\boldsymbol{r}_{ij} \cdot \boldsymbol{m}_j)}{r_{ij}^2} \right), \tag{1.7}$$

with μ_B the Bohr magneton, $\boldsymbol{m}_i$ the magnetic moment of atom i, and $\boldsymbol{r}_{ij}$ the vector pointing from atom i to atom j.

The dipolar interaction contributes [32]:

(a) to the **shape anisotropy**: the energy drops proportionally to $1/r_{ij}^3$, which is rather slow. Magnetic moments in bulk are then significantly influenced by the moments at the surface and, therefore, by the shape of the surface (shape of the magnetic body). The shape anisotropy itself has the form of a volume anisotropy [Eq. (1.3)].

(b) to the **magnetocrystalline anisotropy** by a uniaxial term [Eq. (1.2)], relevant for strained lattice or for interfaces. However, both for strained crystals and for interfaces, the dipolar contribution is rather small compared to the one from spin-orbit coupling [32].

1.5. Spin-orbit coupling effects

The spin-orbit coupling (SOC) is the key ingredient of volume and interface *magnetocrystalline anisotropy*, as well as strain-induced anisotropy [32]. Below, we illustrate this relativistic effect by a semi-classical picture.

Spin-orbit interaction

The spin-orbit coupling links the electron's orbital motion to its spin [30, 33]. It is a relativistic effect and must be derived from the Dirac equation, but in a simplified picture, it may be viewed as a Zeeman interaction. This is illustrated in Fig. 1.3. From the reference frame of an electron orbiting a nucleus, the nucleus is orbiting the electron. This positively charged orbiting nucleus creates a current loop, which induces a magnetic field at its center by the Biot-Savart law. The interaction of this magnetic field with the electron's magnetic moment (its spin) provides an energy contribution due to the *magnetostatic (Zeeman) interaction*.

Thereby, the electron's orbital motion and its spin are coupled. Now, because the spin is coupled to the orbital motion and the orbital motion is coupled to the lattice (by a Coulomb interaction with the surrounding nuclei), *the spin is coupled to the lattice*. The magnetization direction (spin) is therefore related to the crystal axis orientation (lattice). This is the basic idea behind the magnetocrystalline anisotropy [32].

The SOC term is usually added to the Hamiltonian as [32, 34]

$$H_{\text{SOC}} = \xi \boldsymbol{L} \cdot \boldsymbol{S}\,, \tag{1.8}$$

where $\boldsymbol{L}$ and $\boldsymbol{S}$ are respectively the orbital angular momentum and spin angular momentum of the particle, and the *spin-orbit coupling constant* $\xi \approx$ 50-100 meV in $3d$ metals. From Eq. (1.8), it is clear that the direction of $\boldsymbol{L}$ and $\boldsymbol{S}$ are coupled.

Besides being one of the two main sources of magnetic anisotropy, the spin-orbit coupling is also important in many other areas of physics [35]; namely to explain the

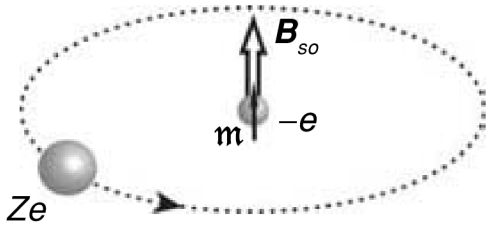

Figure 1.3: Spin-orbit coupling explained by an effective magnetic field ($\boldsymbol{B}_{\mathrm{so}}$), which comes from the orbiting motion of the nucleus around the electron (from the electron's point of view). From [29].

magnetic dichroism, Kerr and Faraday effects [36], in the recently discovered topological insulators [37], when treating optical properties [38] and dealing with heavy elements, and it is partially responsible for the *fine structure* of atoms [29, 39].

1.6. Magnetic anisotropy in data storage

Increasing the information storage *density* requires downsize scaling (shrinking) of the memory bits. To do this, one must increase the magnetic anisotropy energy to retain the same stability against thermal fluctuations [1]. Here, we explain this concept.

Changing the information written in a magnetic memory bit requires external switching of the magnetization from one stable state to the other (up to down or vice versa). To switch, the magnetization must overcome an energy barrier

$$\Delta E = E_{\mathrm{MA}} \cdot S\,, \tag{1.9}$$

where E_{MA} is the anisotropy energy per unit area from Eq. (1.3) and S is the area of the magnetic bit.

Thermal fluctuations may also switch the magnetization *spontaneously*, which results in data loss. On average, this spontaneous switching happens every time interval τ. By the Arrhenius law, the spontaneous switching happens more often (i.e., τ is smaller) when the temperature T is higher [1]

$$\tau = \tau_0 \exp\left(\frac{\Delta E}{k_B T}\right)\,, \tag{1.10}$$

where τ_0 is the characteristic attempt time (≈ 1 ns), and k_B is the Boltzmann constant.

The typical requirement is for the information to stay stable for $\tau = 10$ years at room temperature $T = 300$ K, which by Eq. (1.10) gives the condition [1]

$$\Delta E = E_{\mathrm{MA}} \cdot S > 45 k_B T\,, \tag{1.11}$$

It is hence clear that **downscaling** (decreasing the surface S of the memory bits) **requires increasing the perpendicular anisotropy**.

2. Density functional theory (DFT)

"The underlying physical laws necessary for the mathematical theory of a large part of physics and the whole of chemistry are thus completely known, and the difficulty is only that the exact application of these laws leads to equations much too complicated to be soluble. It, therefore, becomes desirable that ***approximate practical methods*** *of applying quantum mechanics should be developed ..."*
P.A.M. Dirac [40], 1929

Many properties of materials can be predicted without the need of their fabrication and experimental measurements, plainly by designing their structure atom by atom and calculating the ground-state of the electron density in the potential of the atomic nuclei (Fig. 2.1). This is done by solving the Schrödinger or Dirac equation, usually within some approximation. The most popular method to do this is the Density Functional Theory (DFT), developed by Walter Kohn and colleagues and recognized by the Nobel Prize in Chemistry in 1998 [41]. The number of publications concerning DFT doubles every 5-6 years [42]. The following chapter is an introduction to this outstanding method. Refer to [37, 43–45] for other comprehensive introductions.

2.1. Many-body Schrödinger equation

To calculate the properties of matter, we start with the problem of solving the non-relativistic time-independent Schrödinger equation [33, 37]

$$\hat{H}\,|\Psi\rangle = E\,|\Psi\rangle\ , \tag{2.1}$$

where $|\Psi\rangle$ is the many-body wave function, and E is the total energy. The Hamiltonian $\hat{H}$ for a system of electrons and nuclei consists of the electronic kinetic energy $\hat{T}_\mathrm{e}$, the nucleus-electron, electron-electron, and nucleus-nucleus Coulomb interactions $\hat{V}_\mathrm{ext}$, $\hat{V}_\mathrm{int}$, and E_{II}, respectively, and the nuclear kinetic energy $\hat{T}_\mathrm{N}$ [37]

$$\begin{aligned}\hat{H} = &\underbrace{-\frac{\hbar^2}{2m_e}\sum_i \nabla_i^2}_{\hat{T}_\mathrm{e}} \underbrace{-\frac{1}{4\pi\varepsilon_0}\sum_{i,I}\frac{Z_i e^2}{|\boldsymbol{r}_i-\boldsymbol{R}_I|}}_{\hat{V}_\mathrm{ext}} + \underbrace{\frac{1}{2}\frac{1}{4\pi\varepsilon_0}\sum_{i\neq j}\frac{e^2}{|\boldsymbol{r}_i-\boldsymbol{r}_j|}}_{\hat{V}_\mathrm{int}} + \underbrace{\frac{1}{2}\frac{1}{4\pi\varepsilon_0}\sum_{I\neq J}\frac{Z_I Z_J e^2}{|\boldsymbol{R}_I-\boldsymbol{R}_J|}}_{E_{II}} - \\ &\underbrace{-\sum_I \frac{\hbar^2}{2M_I}\nabla_I^2}_{\hat{T}_\mathrm{N}\approx 0}\,,\end{aligned} \tag{2.2}$$

with $\hbar$ the Planck constant, m_e the electron mass, ∇_i^2 the Laplace operator acting on electron i, ε_0 the vacuum permittivity, Z_I the charge of nucleus I, e the elementary

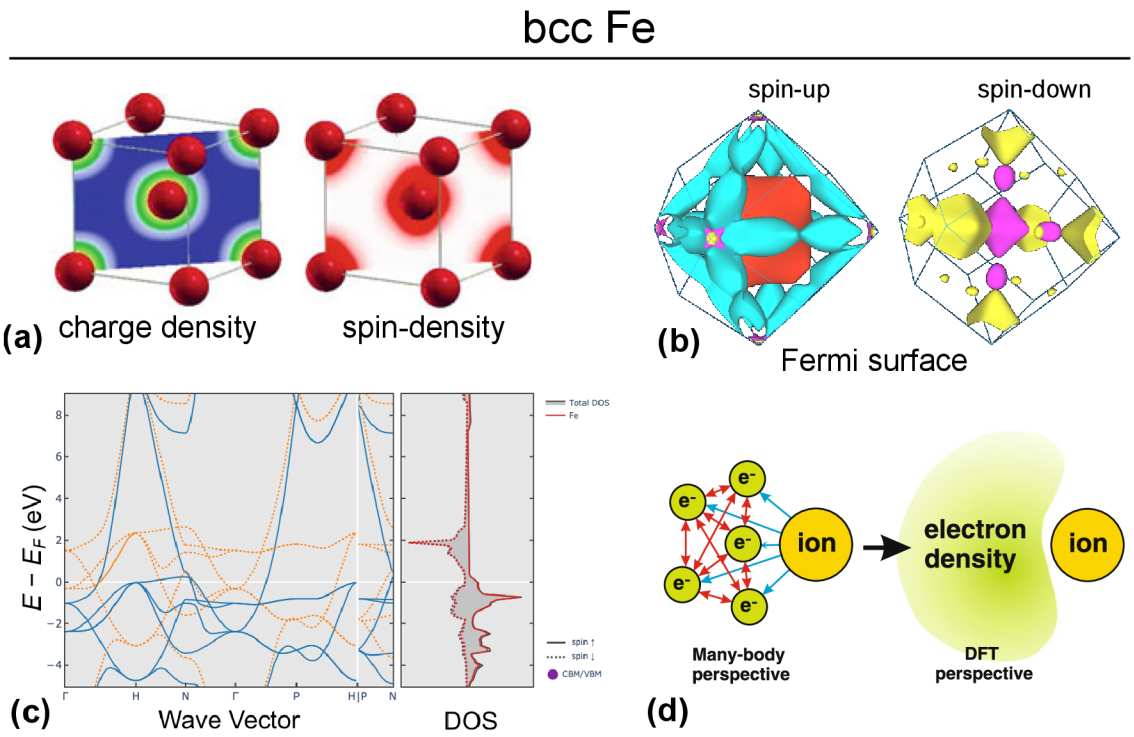

Figure 2.1: (a) The electron (charge) and the magnetization (spin) density of bcc Fe [46]. (b) The Fermi surface in the Brillouin zone of bcc Fe [47]. (c) Band structure and Density of States (DOS) of bcc Fe [48]. (d) The many-body vs. the density approach [49].

charge, $\boldsymbol{r}_i$ the position of electron i, $\boldsymbol{R}_I$ the position of nucleus I, M_I the mass of nucleus I, and ∇_I^2 the Laplace operator acting on nucleus I. The equation disregards the small relativistic effects such as spin-orbit coupling (Sec. 1.5).

Atomic units

Except for Eq. (2.2), which we have kept in SI units, in the rest of the text we use the Hartree atomic units [50], where by definition $\hbar = e = a_0 = m_e = 1$, where a_0 is the Bohr radius. It also follows[1] that $1/4\pi\varepsilon_0 = 1$. Using the atomic units, the kinetic energy operator and the electron Coulomb potential simplify as

$$\begin{aligned} \hat{T}_\mathrm{e} &= -\frac{\hbar^2}{2m_e}\nabla^2 \quad \rightarrow \; -\frac{1}{2}\nabla^2 \,, \\ V_\mathrm{Coulomb} &= -\frac{e}{4\pi\varepsilon_0 r} \quad \rightarrow \; -\frac{1}{r} \,. \end{aligned} \tag{2.3}$$

2.2. Born-Oppenheimer approximation

The first step of tackling problem Eq. (2.1)-Eq. (2.2) is to use the excellent *Born-Oppenheimer* (*adiabatic*) approximation [51], which says that the wave functions of electrons and nuclei can be treated separately. Since nuclei are much heavier than electrons ($M_I \approx 2000\, m_e$), the electrons can react very fast and hence are always in their instantaneous ground state,

[1] from the expression for Bohr radius, $a_0 = 4\pi\varepsilon_0\hbar^2/m_e e^2$

regardless of the (slow) nuclear motion. Then $|\Psi\rangle$ in Eq. (2.1) represents only the (many-body) electronic wave function; for the nuclear wave function, there is a separate equation, which can be used, for instance, for calculations of phonons [37]. Since $1/M_I$ is small, the nuclear kinetic energy $\hat{T}_\mathrm{N}$ from Eq. (2.2) is neglected (≈ 0). The Coulomb nucleus-nucleus interaction E_{II} is simply an additive constant to the total energy.

2.3. Hartree-Fock approximation

Even after separating the motion of electrons and nuclei, it is impossible to solve Eq. (2.2) analytically, since the large number of electrons[2] interact with each other via the Coulomb interaction $\hat{V}_\mathrm{int}$. This makes the task a *Many Body Problem* [52].

The problem was first tackled *numerically* by Hartree in 1927 [50] and extended by Fock [53] and Slater [54]. The *Hartree-Fock approximation* assumes that the many-electron wave function can be replaced by a linear combination of single-electron (non-interacting) wave functions. Working with non-interacting electrons greatly simplifies the problem, and the reason why this approach is physically sensible is the electron *screening* [55]. We return to this point right below when discussing the exchange-correlation hole.

The Hartree-Fock approach also replaces the problematic electron-electron interaction $\hat{V}_\mathrm{int}$ by a much simpler term, which suggests that the electron wave functions interact with each other in the same way as the total electron charge density interacts with itself via the Coulomb interaction[3]. This term is called the *Hartree energy*

$$E_\mathrm{H} = \frac{1}{2}\int \mathrm{d}^3r\,\mathrm{d}^3r'\,\frac{n(\boldsymbol{r})n(\boldsymbol{r'})}{|\boldsymbol{r}-\boldsymbol{r'}|}\,, \tag{2.4}$$

where the electron density

$$n(\boldsymbol{r}) = |\Psi(\boldsymbol{r})|^2\,. \tag{2.5}$$

When integrated over, $n(\boldsymbol{r})$ must add up to the total number of electrons N

$$N = \int \mathrm{d}^3r\; n(\boldsymbol{r})\,. \tag{2.6}$$

Note, however, that by approximating $\hat{V}_\mathrm{int}$ with E_H, we neglect[4] two important many-electron effects: *exchange* and *correlation*.

2.4. Exchange-correlation hole

Imagine first what happens if we bring an electron with charge $q = -e$ in vacuum close to a conductive plane [Fig. 2.2(b)].

The electrons at the conductive surface are repelled, and there is a net positive charge, which has the same electrostatic field as if the electron had a mirror image with opposite charge $-q = e$ below the surface. (This is the electrostatic *method of images* [57].)

Decreasing the separation x [Fig. 2.2(b)], the electron and its positive mirror image approach each other, until at $x \approx$ 1-2 Å, the electron wave function starts to overlap with

[2] typically 10^{23} electrons/cm^3 in a solid

[3] the $1/4\pi\epsilon_0$ prefactor is dropped since we are using atomic units,

[4] The exchange, originally missing in the Hartree method, was added by Fock [53]. Correlation is added in post-Hartree-Fock methods [56].

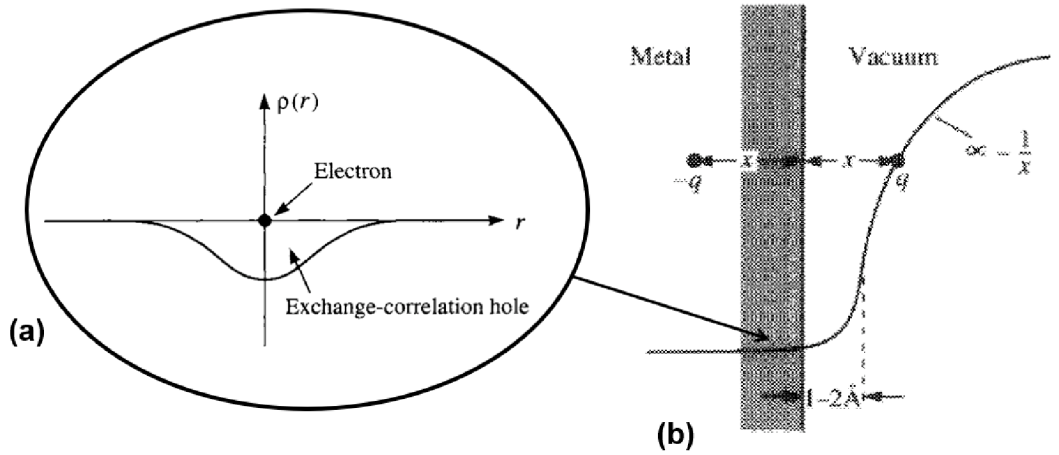

Figure 2.2: (a) The negative electron density n_{xc} surrounding an electron is called an *exchange-correlation* hole [55]. (b) Illustration of the origin of n_{xc}: bringing an electron close to a conductive plane creates a positively charged mirror hole. At $x = 0$, the hole surrounds the electron [55].

the electron wave functions at the surface [55]. The system energy then deviates from the expected classical $E \propto -\frac{1}{x}$ (it does not diverge to minus infinity) and once the electron enters the conductor, the positive mirror point charge surrounds the electron, forming an *exchange-correlation hole* [Fig. 2.2(a)].

An exchange-correlation hole $n_{\mathrm{xc}}(\boldsymbol{r})$ is a negative electron density (therefore a hole) surrounding an electron. It consists of the exchange and correlation part

$$n_{\mathrm{xc}} = n_{\mathrm{x}} + n_{\mathrm{c}}\,, \tag{2.7}$$

and the two are distinct in their nature.

1. The **exchange hole** $n_{\mathrm{x}}(\boldsymbol{r})$ accounts for two facts. Firstly, electrons of the same spin in the same quantum state cannot be at the same time at the same place, obeying the Pauli exclusion principle. Thereby, n_{x} affects electrons with the same spin.

   Second, n_{x} corrects for the wrong notion entrenched in the Hartree energy expression [Eq. (2.15)] that an electron interacts with *itself*. For example, in a hydrogen atom, where there is only one electron, n_{x} completely cancels the density of the one present electron to avoid this *self-interaction* [37, Sec. 3.7]. Hence, in hydrogen, the exchange hole represents minus one electron. In fact, it is a general feature of the exchange hole that its integral is exactly minus one electron [58]

   $$\int n_{\mathrm{x}}(\boldsymbol{r})\,\mathrm{d}^3 r = -1\,. \tag{2.8}$$

2. On the other hand, integral over the **correlation hole** $n_{\mathrm{c}}(\boldsymbol{r})$ is zero

   $$\int n_{\mathrm{c}}(\boldsymbol{r})\,\mathrm{d}^3 r = 0\,, \tag{2.9}$$

   so it only serves to *redistribute* the hole's density. The correlation hole n_{c} corrects for the fact that interacting electrons are not independent – their joint density

is correlated[5]. Unlike exchange, correlation is also important for interactions of electrons with opposite spins.

Later, we will introduce the exchange-correlation energy E_{xc}, very important in density functional theory. It can be viewed as an attractive Coulomb interaction between the electron density n and the exchange-correlation hole n_{xc}.

2.5. Thomas-Fermi method

The original *density functional theory* was proposed separately by Thomas [59] and Fermi [60] in 1927. They approximated both the electron-electron interaction *and* the kinetic energy of electrons as a *functional* of the electron density n. A *functional*, is a rule for mapping a function to a number, just as a function is a rule for mapping a number to a different number [43]. A quantity Q, which is the functional of another quantity n is denoted $Q[n]$.

Hence, all terms in the Thomas-Fermi total energy $E_{\mathrm{TF}}[n]$ depend on the density; they are integrals of the density. The expressions are based on analytic formulae for the homogeneous free electron gas (see Eq. (6.1) in Ref. [37] for details.). The correct density $n(\boldsymbol{r})$ is the one which minimizes $E_{\mathrm{TF}}[n]$, subject to the constraint that the total number of electrons N is correct [Eq. (2.6)].

Just as Hartree and Fock, Thomas and Fermi also neglected the exchange and correlation between electrons[6].

The argument to create an approximation based on electron density instead of electron wave functions is straightforward. The many-body electron wave function for N electrons depends on $3N$ variables (3 spatial coordinates x, y, and z for each electron). On the other hand, the electron *density* $n(\boldsymbol{r})$ is a function of only three spatial coordinates. And in fact, as shown in the next Sec. 2.6, all the properties of a system can, indeed, be determined purely from its ground-state electron density.

Although significant, the Thomas-Fermi model is too crude to be widely used in practice [63] and a more sophisticated approach was needed. An approach, which is formally exact but leaves a lot of space for effective approximations.

2.6. Hohenberg-Kohn theorems

The modern formulation of density functional theory started with two important theorems proved by Pierre Hohenberg and Walter Kohn in 1964. They provide a reformulation of the many-body problem Eq. (2.1)-Eq. (2.2) in terms of functionals of the electron density.

[5] In mathematical terms, the joint density $n(\boldsymbol{r}, \sigma; \boldsymbol{r'}, \sigma')$ of finding one electron with spin σ at point $\boldsymbol{r}$ and a different electron of spin σ' at point $\boldsymbol{r'}$ is the sum of two terms: (1) the simple, uncorrelated, product of the independent densities of the two electrons and (2) the exchange correlation hole [37]

$$n(\boldsymbol{r}, \sigma; \boldsymbol{r'}, \sigma') = n(\boldsymbol{r}, \sigma)\, n(\boldsymbol{r'}, \sigma') + n_{\mathrm{xc}}(\boldsymbol{r}, \sigma; \boldsymbol{r'}, \sigma')\,, \tag{2.10}$$

[6] An extension by Dirac added the local approximation for exchange interaction [61], still in use today and discussed in Sec. 2.9. The correlation between electrons is neglected altogether. Correction for the kinetic energy in nonhomogeneous systems taking into account also the gradient of the density, not just the density itself, was proposed by Weizsacker [62].

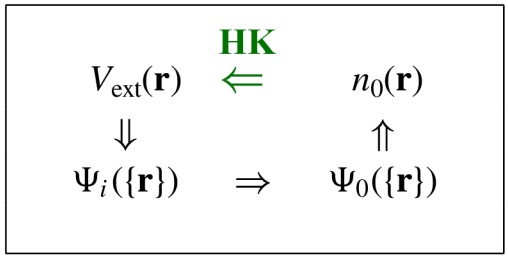

Figure 2.3: The ground-state density n_0 of interacting electrons in an external potential can be considered as the "basic variable". As proved by Hohenberg and Kohn, from n_0 we can get the external potential $V_{\text{ext}}(\boldsymbol{r})$ which produced it. From $V_{\text{ext}}(\boldsymbol{r})$, we can in principle calculate the eigenstates $\Psi_i(\{\boldsymbol{r}\})$, including the groundstate $\Psi_0(\{\boldsymbol{r}\})$. Hence, all properties of a system are unique functionals of its ground-state density. Adapted from [37].

The Hohenberg-Kohn (HK) theorems state that [64]:

1. **All the properties of an interacting system of electrons are determined from its ground-state density n_0.**

   In fact, the theorem states that from the ground-state density n_0 one can *uniquely*[7] determine the external potential $V_{\text{ext}}(\boldsymbol{r})$ (which generated this ground-state density)[8]. From $V_{\text{ext}}(\boldsymbol{r})$, one can then in principle calculate the electron many-body wave function $\Psi(\{\boldsymbol{r}\})$, both ground-state and excited, and hence calculate all the system's properties.

   The theorem goes from the solution (n_0) back to the problem ($V_{\text{ext}}(\boldsymbol{r})$) back to the solution ($\Psi_0(\{\boldsymbol{r}\})$). This is shown schematically in Fig. 2.3. However, this information by itself is not very useful. It does not answer how to get $\Psi_i(\{\boldsymbol{r}\})$ from V_{ext}, which is the ultimate problem.

2. **The correct ground-state density n_0 is obtained by minimizing the system's total energy $E[n]$**, which can be prescribed as a functional of n universally, independent of the external potential $V_{\text{ext}}(\boldsymbol{r})$.

To make full use of the HK theorems, the Kohn-Sham scheme is often used and will be presented in the next Section 2.7.

Note that Levy and Lieb [65–67] later established an alternative formulation to Hohenberg-Kohn theorems. Their *Constrained Search Formulation* of DFT is more general and in many cases more instructive [37].

HK theorems can be generalized [37] to include:

I. the electron spin [68], by treating separately the densities for spin-up and spin-down electrons (*spin density functional theory*). To account for the effects of magnetic field on the orbital motion of the electrons, not only on their spin, it is needed to consider also the electronic current, not only charge [69]. This makes the problem relativistic.

[7] except for an (unimportant) additive constant

[8] In DFT, the external potential $V_{\text{ext}}(\boldsymbol{r})$ is usually equivalent to the Coulomb potential from the nuclei, see Eq. (2.2).

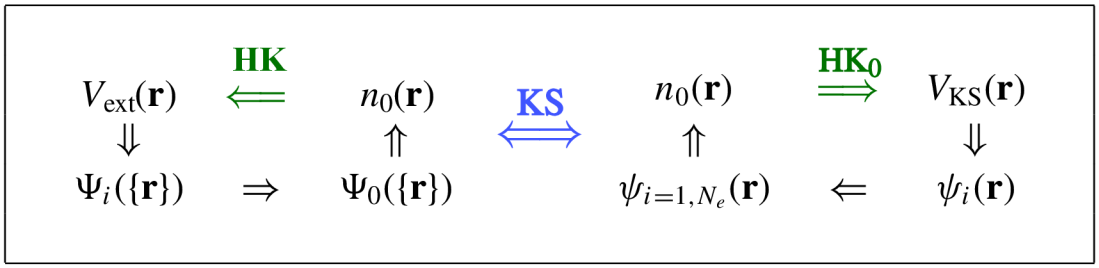

Figure 2.4: The KS mapping of the real problem onto one-electron problem. The left half corresponds to Fig. 2.3. Adapted from [37].

II. thermal equilibrium properties, such as specific heat or entropy, as shown by Mermin [70]. The Mermin functional is not widely used, though, because it is difficult to formulate. It must include electron properties beyond the ones of Hohenberg-Kohn's functional [37].

III. time-dependent problems, as shown by Runge and Gross [71].

IV. external electric fields and electric polarization [72].

2.7. Kohn-Sham equations

The HK theorems say that all you need is electron density. But there are many difficulties when leaving out the wave function and working purely with the density[9]. For instance, there is no known way to get the kinetic energy directly from the density [37]. Also, it is hard to tell if a system is ionic or neutral, looking only at the density [73].

The Kohn-Sham approach [74] returns the wave function back into play, side-by-side with the density.

The **assumption of Kohn and Sham** is that the real ground-state density n_0 can be written as a sum over the densities of a certain number of non-interacting (free) electrons (Fig. 2.4). Each free electron i has some spin $\sigma \in \{\uparrow,\downarrow\}$ and some wave function $\psi_i^\sigma(\boldsymbol{r})$. If N^σ is the number of electrons for spin σ, the ground-state density

$$n_0(\boldsymbol{r}) = n_0^\uparrow(\boldsymbol{r}) + n_0^\downarrow(\boldsymbol{r}) = \sum_{i=1}^{N^\uparrow} |\psi_i^\uparrow(\boldsymbol{r})|^2 + \sum_{i=1}^{N^\downarrow} |\psi_i^\downarrow(\boldsymbol{r})|^2 \,. \tag{2.11}$$

So the electrons are treated a priori as non-interacting, and the electron-electron interaction is represented by the Hartree energy [Eq. (2.15)] and a small energy term $E_{\text{xc}}[n]$, which encompasses all the electron-electron interaction effects, which Hartree energy neglects.

The **Kohn-Sham energy**, which needs to be minimized, then writes

$$\boxed{E_{\text{KS}}[n] = T_{\text{s}}[n] + E_{\text{ext}}[n] + E_{\text{Hartree}}[n] + E_{\text{xc}}[n] + E_{II}}\,, \tag{2.12}$$

[9] the squared modulus of the wave function

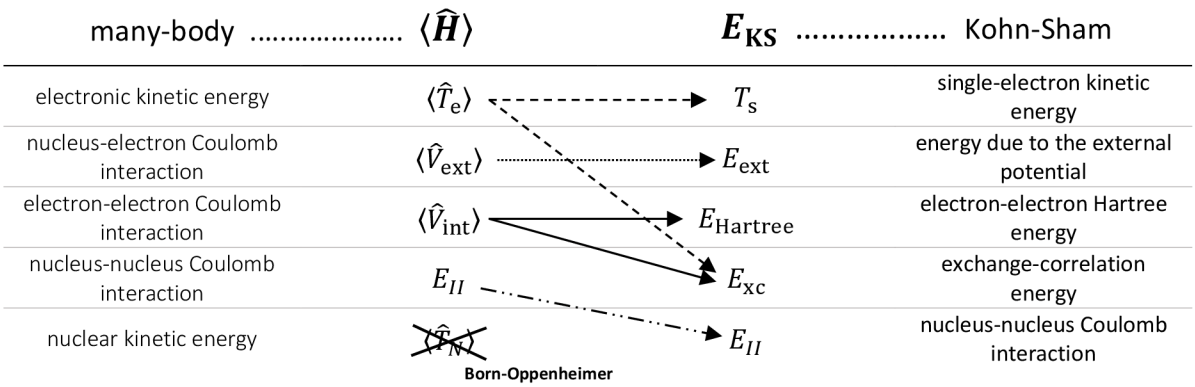

Figure 2.5: Comparing the expectation value of the original many-body Hamiltonian [Eq. (2.2)] and the Kohn-Sham energy [Eq. (2.12)]. The part of the original electronic kinetic energy and electron-electron Coulomb interaction, which comes from the complicated many-body effects is encompassed in the exchange-correlation energy, following Eq. (2.16). Different line styles are used only for clarity.

where the single-electron kinetic energy

$$T_\mathrm{s} = -\frac{1}{2} \sum_\sigma \sum_{i=1}^{N^\sigma} \langle \psi_i^\sigma | \nabla^2 | \psi_i^\sigma \rangle \ , \tag{2.13}$$

the energy due to the external potential (the Coulomb potential of the nuclei)

$$E_\mathrm{ext}[n] = \int \mathrm{d}^3\boldsymbol{r}\, V_\mathrm{ext}(\boldsymbol{r}) n(\boldsymbol{r}) \, , \tag{2.14}$$

the electron-electron Hartree energy

$$E_\mathrm{Hartree}[n] = \frac{1}{2} \int \mathrm{d}^3 r \, \mathrm{d}^3 r' \, \frac{n(\boldsymbol{r}) n(\boldsymbol{r}')}{|\boldsymbol{r} - \boldsymbol{r}'|} \, , \tag{2.15}$$

the *exchange-correlation energy* E_xc corrects for the fact that the true kinetic energy $\langle \hat{T}_\mathrm{e} \rangle$ is different from the sum of the single-electron kinetic energies $T_\mathrm{s}[n]$ (due to correlation effects) and the electron-electron interaction energy $\hat{V}_\mathrm{int}$ is different from the mean-field Hartree energy $E_\mathrm{Hartree}[n]$ (due to exchange and correlation effects)

$$E_\mathrm{xc}[n] = \overbrace{\langle \hat{T}_\mathrm{e} \rangle - T_\mathrm{s}[n]}^{\Delta T_\mathrm{correlation}} + \overbrace{\langle \hat{V}_\mathrm{int} \rangle - E_\mathrm{Hartree}[n]}^{\Delta V_\mathrm{exchange\text{-}correlation}} \, . \tag{2.16}$$

See Eq. (2.2) for definitions of the electron kinetic energy operator $\hat{T}_\mathrm{e}$ and the electron-electron interaction energy $\hat{V}_\mathrm{int}$.

Finally, the constant nucleus-nucleus Coulomb interaction E_{II} must be added for completeness.

Note that Eq. (2.12) is *in principle exact*. For a given distribution of nuclei (external potential $V_\mathrm{ext}(\boldsymbol{r})$) and a given density n, all terms except E_xc are well-known and straightforward to calculate. The unknown part, $E_\mathrm{xc}[n]$, constitutes only a small energy contribution. How to express $E_\mathrm{xc}[n]$ with powerful approximations is explained in Sec. 2.9.

In Fig. 2.5, we compare the Kohn-Sham energy [Eq. (2.12)] and the expectation value of the original many-body Hamiltonian [Eq. (2.2)].

Applying the variational principle to E_{KS} with respect to the wave functions, one arrives at the **Kohn-Sham Schrödinger-like equation** [37]

$$\boxed{H_{\mathrm{KS}}\,\psi_i(\boldsymbol{r}) = \varepsilon_i\,\psi_i(\boldsymbol{r})}\,, \tag{2.17}$$

with the Kohn-Sham effective Hamiltonian

$$H_{\mathrm{KS}} = -\frac{1}{2}\nabla^2 + V_{\mathrm{eff}}(\boldsymbol{r})\,, \tag{2.18}$$

where instead of the energies E from Eq. (2.12) we now have their respective potentials $V \equiv \frac{\delta E}{\delta n(\boldsymbol{r})}$

$$V_{\mathrm{eff}}(\boldsymbol{r}) = V_{\mathrm{ext}}(\boldsymbol{r}) + V_{\mathrm{Hartree}}(\boldsymbol{r}) + V_{\mathrm{xc}}(\boldsymbol{r})\,. \tag{2.19}$$

For a given arrangement of nuclei (given external potential $V_{\mathrm{ext}}(\boldsymbol{r})$), we solve the Kohn-Sham problem Eq. (2.17)-Eq. (2.19), thereby obtaining the Kohn-Sham wavefunctions $\psi_i(\boldsymbol{r})$, which give us the ground-state density n_0 via Eq. (2.11). From n_0 we get the system's total energy via Eq. (2.12) and, in principle (Sec. 2.6), also any other property of the system.

Let us take a closer look at how to solve the Kohn-Sham problem Eq. (2.17)-Eq. (2.19).

2.8. Self-consistent cycle

Since the Kohn-Sham Hamiltonian H_{KS} depends on the density, which actually follows from that Hamiltonian in the first place, the Kohn-Sham equation needs to be solved in a self-consistent iterative manner. The algorithm is depicted in Fig. 2.6. With the electron density from some initial guess, the effective potential V_{eff} [Eq. (2.19)] is calculated. From the KS equation [Eq. (2.17)], we then get the KS wave functions $\psi_i^\sigma(\boldsymbol{r})$. From the KS wave functions, we calculate the density n and iterate until the self-consistent cycle output density n_{out} and input density n_{in} are not close enough. The criterion is usually that the change in the total energy in the subsequent iterative steps is below certain threshold[10] E_{diff}

$$E_{\mathrm{KS}}^{i+1} - E_{\mathrm{KS}}^{i} < E_{\mathrm{diff}}\,. \tag{2.20}$$

Mixing

For the self-consistent cycle [Fig. 2.6] to converge, and converge fast, one cannot simply use n_{out}^i as the input for the next cycle n_{in}^{i+1} [75]. Most often, a linear combination of the new and the original density is used [37]

$$n_{\mathrm{in}}^{i+1} = \alpha n_{\mathrm{out}}^{i} + (1-\alpha) n_{\mathrm{in}}^{i}\,, \tag{2.21}$$

where generally $0 < \alpha \leq 1$, but in fact, to ensure convergence, the upper limit for α is usually much more strict [76]. This linear mixing works well for insulators. For metals,

[10] $E_{\mathrm{diff}} \sim 10^{-7}$ eV

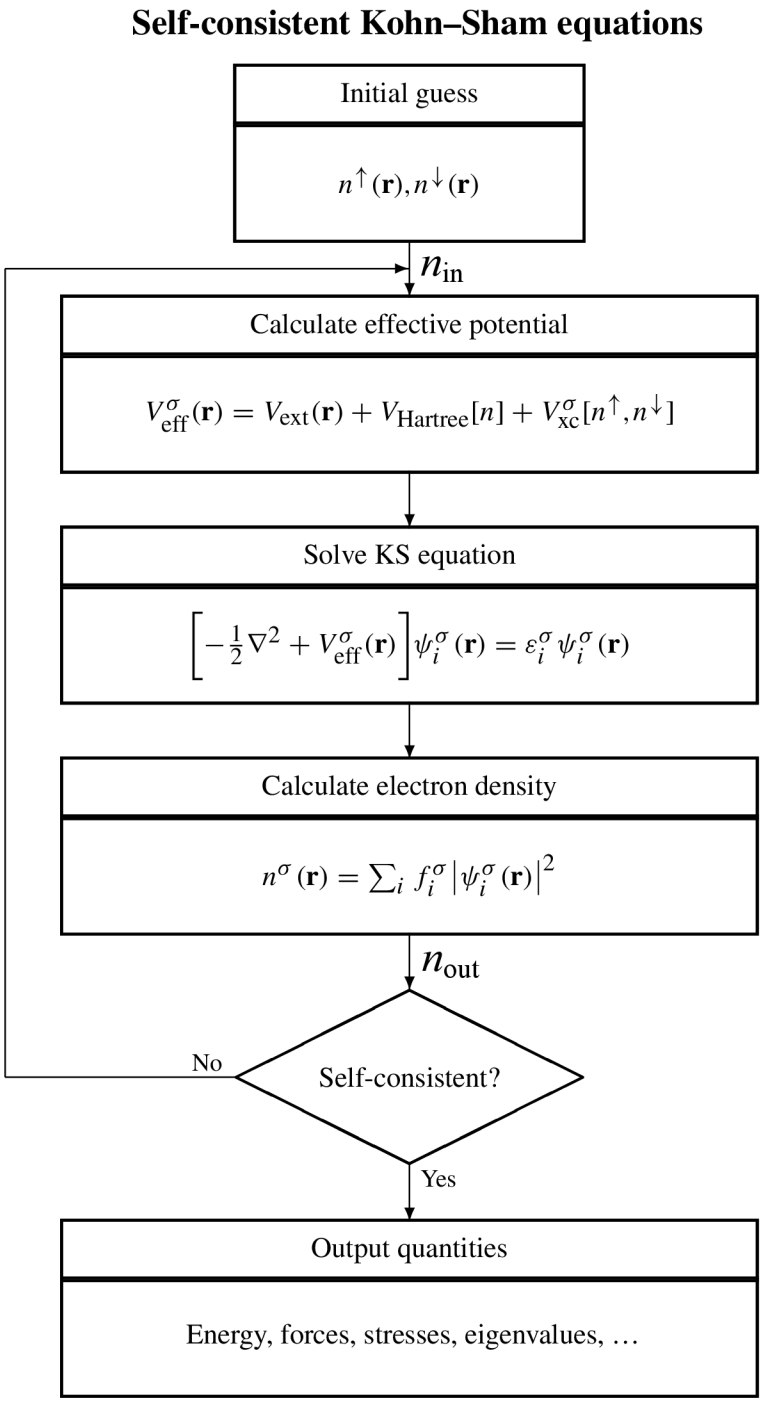

Figure 2.6: The self-consistent cycle algorithm for solving the Kohn-Sham equations Eq. (2.17). Often used for the initial guess is simply the sum of electron densities from all the atoms in the system, as if they were isolated. From [37].

however, values as low as $\alpha \approx 0.01$ may be necessary for convergence [75], making the convergence slow and the number of necessary cycles large. Therefore, more sophisticated mixing schemes have been developed, such as the Broyden method [77], where α is not constant but updated dynamically at each iterative step. See Ref. [78] for other advanced mixing methods.

2.9. Exchange-correlation functionals

Density functional theory owes its success to the fact that the difficult term in Eq. (2.12) – the exchange-correlation energy E_{xc} – can be approximated remarkably well using surprisingly simple expressions. In this Section, we introduce the two simplest: the local (LDA) and the semilocal (GGA) approximation.

Local density approximation (LDA) functional

The first step towards expressing E_{xc} was already taken by Kohn and Sham themselves in their seminal paper [74]. Their *local density approximation* (LDA) assumes that each point in space contributes to E_{xc} like a little amount of free electron gas of the same density n. The exchange-correlation energy $\epsilon_{\mathrm{xc}}^{\mathrm{hom}}(n)$ for a free electron gas of given density n is known[11]. Hence, [37, 74]

$$E_{\mathrm{xc}}^{\mathrm{LDA}}[n] = \int \mathrm{d}^3 r \, n(\boldsymbol{r}) \, \epsilon_{\mathrm{xc}}^{\mathrm{hom}}(n(\boldsymbol{r})) \,. \tag{2.22}$$

Because the functional does not consider any interaction between the neighboring free-electron-like infinitesimal regions, the approximation is called *local* and is naturally best for slowly varying densities. Surprisingly, even for extremely inhomogeneous cases like the hydrogen atom, it gives binding energy with the accuracy of $\approx 7\%$ [37].

The functional is simple yet successful because it preserves the sum rules [Eq. (2.8) and Eq. (2.9)], which must always hold for the exchange-interaction hole [81], and because the precise shape of the exchange-correlation hole is, in fact, not crucial, only its spherical average [82].

Still, LDA is limited in many senses. Its general shortcoming is that it predicts too large bonding energies and too short bond lengths [83].

Generalized gradient approximation (GGA) functional

Improved results compared to LDA are obtained by also including the gradient of the density ∇n, not only the density itself [35]

$$E_{\mathrm{xc}}^{\mathrm{GGA}}[n] = \int \mathrm{d}^3 r \, n(\boldsymbol{r}) \, \epsilon_{\mathrm{xc}}^{\mathrm{hom}}(n(\boldsymbol{r})) \, F_{\mathrm{xc}}(n(\boldsymbol{r}), |\nabla n(\boldsymbol{r})|) \,, \tag{2.23}$$

where F_{xc} is an enhancement factor encompassing the density gradient; the functional is therefore *semilocal*.

[11] The exchange-correlation energy can be divided into its exchange and correlation part [74] $\epsilon_{\mathrm{xc}}^{\mathrm{hom}}(n) = \epsilon_{\mathrm{x}}^{\mathrm{hom}}(n) + \epsilon_{\mathrm{c}}^{\mathrm{hom}}(n)$. The exchange energy for a homogeneous electron gas $\epsilon_{\mathrm{x}}^{\mathrm{hom}}$ is given analytically [61], while the correlation $\epsilon_{\mathrm{c}}^{\mathrm{hom}}$ has been calculated very precisely by Monte Carlo methods [79] and parametrized by Perdew and Zunger [80].

Including ∇n corrects the bonding energy, although it may somewhat overcorrect the bond lengths [83]. There are three widely utilized GGA functionals [84–86]. In this work, we use the one by Perdew, Burke, and Ernzerhof (PBE) [87].

Advanced functionals

While GGA improves some deficiencies of LDA, it does not account, e.g., for van der Waals interactions [37]. There are many advanced functionals beyond GGA, which might depend not only on the density but also on the wave functions, involve the *kinetic energy density*, or be able to treat localized d and f orbitals with strong interactions [37, 88].

2.10. Plane-wave basis and PAW method

In practice, the density and wave functions must be represented in a certain basis. In Density Functional Theory, three bases are often used [37]:

1. **Plane wave basis and discrete grids.** Plane waves [39] have many advantages: they arise naturally in quantum mechanics; they naturally obey the Bloch theorem of solid-state physics; they are independent of the positions of nuclei; forces on atoms are numerically exact derivatives of the total energy, and the basis can be systematically improved by including waves with ever-higher spatial frequency [37, 89].

   In addition, a transition from the plane-wave basis (the *reciprocal space*) to the *discrete grid basis* [90] (the *real space*) can be made very efficiently via the Fast Fourier Transform. This is very useful since some calculations are easily done in the real space[12], while others in the reciprocal space[13]. We can also exploit the combination of the two bases, as done in the Projector Augmented Wave (PAW) method [91] described below, where *part* of the space is treated with plane waves and the other part with discrete grids.

2. **Localized orbitals.** Functions resembling atomic orbitals and centered at the nuclei are used [92]. This basis is more suitable for computational chemistry to describe localized individual molecules, in contrast with solid-state physics, where we usually deal with periodic systems.

3. **Atomic sphere methods.** The idea here is to divide the space into regions near the nuclei (atomic spheres), inside which the wave function oscillates quite rapidly, and the interatomic region, where it oscillates much more slowly. Smooth functions are used as a basis in the interatomic region and they are *augmented* in the atomic spheres. These are the Linearized Augmented Plane Wave (LAPW) method [93, 94], Korringa-Kohn-Rostoker (KKR) method[14] [95, 96] and Linearized Muffin-tin Orbitals (LMTO) method [97].

In addition, there are *linear scaling methods* [98], which are suitable for large systems (e.g., a fragment of an RNA molecule with $\approx$ 1000 atoms [98]). Using them, the computation time then scales linearly with the number of atoms N, while in the previous

[12] e.g., calculating the density from the wave functions
[13] the kinetic energy calculation
[14] also called Green's function method or multiple-scattering theory (MST)

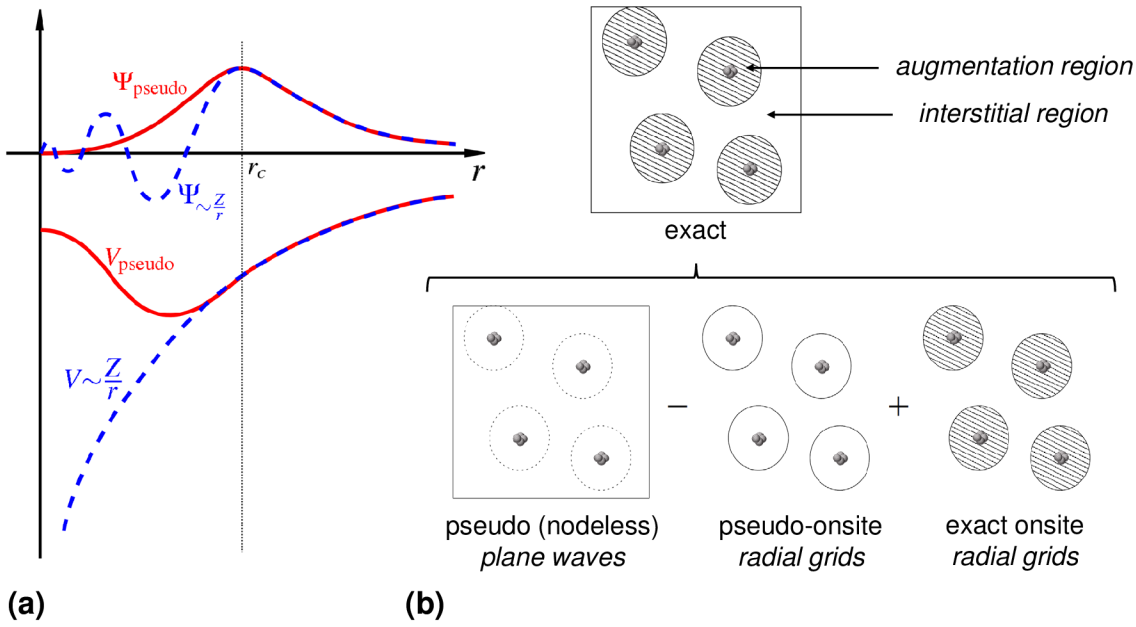

Figure 2.7: (a) Inside a sphere of a cutoff radius r_c from the given nucleus, a *pseudopotential* V_{pseudo} replaces the real Coulomb potential V to suppress rapid oscillations in the wavefunction Ψ. Above r_c, the exact and pseudized potentials and wavefunctions are equal. The region $r < r_c$ is called the *augmentation region*. The region $r > r_c$ is called the *interstitial region*. From [101]. (b) The exact Kohn-Sham wave functions in the PAW method consist of three terms. A combination of plane-wave basis and radial grids is exploited. The wavefunction and its derivative is assured to be continous at the sphere boundaries [35]. Adapted from [102].

three cases, it scales as N^2 or N^3 [37]. On the other hand, care must be taken to ensure accurate results.

Pseudopotentials

Near a nucleus, the Coulomb potential $V \propto -\frac{1}{r}$ is strong and it forces the wave functions to oscillate rapidly [37], see Fig. 2.7(a). When using the plane-wave basis, high spatial frequencies must be included to describe these rapid oscillations. On the other hand, this strong Coulomb potential near the nucleus influences mainly the core electrons, which do not respond significantly to the neighboring atoms[15] and hence are often approximated as non-changing: the so-called *frozen core approximation* [99].

A *pseudopotential* replaces the strong Coulomb potential near a nucleus with a potential that is much weaker, to suppress rapid oscillations in the wave function [55, 100]. Further away from the nucleus, the pseudopotential has its value equal to the true Coulomb potential, see Fig. 2.7(a). The new wave function is called a *pseudo wave function*, which has the correct form far from the nucleus but does not oscillate rapidly close to the nucleus. Thereby, high-frequency plane waves are not needed, and the required size of the plane-wave basis is smaller.

[15] do not take part in chemical bonds

Projector augmented waves (PAW)

The Projector Augmented Wave (PAW) method [91] is a modern method, which efficiently treats the behavior of wave functions both near the nucleus and between the atoms. The unit cell [top part of Fig. 2.7(b)] is divided into two regions:

I. Augmentation spheres, which are centered on atomic nuclei, with a cut-off radius r_c^a for a given atom a. In this region, the Coulomb potential is strong, and the wave functions, which oscillate rapidly, are represented by localized orbitals.

II. Interstitial region in-between the spheres. In this region, the Coulomb potential is already weak, and the wave functions, which oscillate slowly, are expanded into plane waves.

The exact wave functions (as well as the densities and energies) then consist of three parts [35, 37], see the bottom part of Fig. 2.7(b): the pseudo wavefunction evaluated with plane waves *minus* the same pseudo wavefunction inside the augmentation sphere evaluated with radial grids *plus* the exact wavefunction in the augmentation sphere evaluated with radial grids.

2.11. Spin-dependent Kohn-Sham equation

To explicitly include **magnetization** into DFT, the wave function is decomposed into its spin-up and spin-down parts [68, 103], together forming a *spinor*[16] ψ and a spin-density $\boldsymbol{s}$ [46]

$$\psi(\boldsymbol{r}) = \begin{pmatrix} \psi_\uparrow(\boldsymbol{r}) \\ \psi_\downarrow(\boldsymbol{r}) \end{pmatrix}; \quad \boldsymbol{s}(\boldsymbol{r}) = \langle \psi(\boldsymbol{r}) | \underline{\boldsymbol{\sigma}} | \psi(\boldsymbol{r}) \rangle \ , \tag{2.24}$$

where $\underline{\boldsymbol{\sigma}} = (\underline{\sigma_x}, \underline{\sigma_y}, \underline{\sigma_z})$ is the vector of Pauli matrices

$$\underline{\sigma_x} = \begin{pmatrix} 0 & 1 \\ 1 & 0 \end{pmatrix}, \quad \underline{\sigma_y} = \begin{pmatrix} 0 & -i \\ i & 0 \end{pmatrix}, \quad \underline{\sigma_z} = \begin{pmatrix} 1 & 0 \\ 0 & -1 \end{pmatrix}. \tag{2.25}$$

The density is treated as a matrix containing both particle and spin density [46]

$$\underline{n}(\boldsymbol{r}) = \begin{pmatrix} \psi_\uparrow^*(\boldsymbol{r})\,\psi_\uparrow(\boldsymbol{r}) & \psi_\uparrow^*(\boldsymbol{r})\,\psi_\downarrow(\boldsymbol{r}) \\ \psi_\downarrow^*(\boldsymbol{r})\,\psi_\uparrow(\boldsymbol{r}) & \psi_\downarrow^*(\boldsymbol{r})\,\psi_\downarrow(\boldsymbol{r}) \end{pmatrix} = \frac{1}{2} \begin{pmatrix} n(\boldsymbol{r}) + s_z(\boldsymbol{r}) & s_x(\boldsymbol{r}) - i s_y(\boldsymbol{r}) \\ s_x(\boldsymbol{r}) + i s_y(\boldsymbol{r}) & n(\boldsymbol{r}) - s_z(\boldsymbol{r}) \end{pmatrix}. \tag{2.26}$$

The **spin-polarized Kohn-Sham equation** is then [46]

$$\left[\left(-\frac{1}{2}\nabla^2 + V_{\text{ext}}(\boldsymbol{r}) + V_{\text{Hartree}}(\boldsymbol{r}) \right) \underline{I} + \underline{V}_{\text{xc}}(\boldsymbol{r}) - \underline{\boldsymbol{\sigma}} \cdot \boldsymbol{B}(\boldsymbol{r}) \right] \begin{pmatrix} \psi_i^\uparrow(\boldsymbol{r}) \\ \psi_i^\downarrow(\boldsymbol{r}) \end{pmatrix} = \varepsilon_i \begin{pmatrix} \psi_i^\uparrow(\boldsymbol{r}) \\ \psi_i^\downarrow(\boldsymbol{r}) \end{pmatrix}, \tag{2.27}$$

where the unit matrix $\underline{I} = \begin{pmatrix} 1 & 0 \\ 0 & 1 \end{pmatrix}$, the exchange correlation matrix $\underline{V}_{\text{xc}} = \frac{\partial E_{\text{xc}}}{\partial \underline{n}(\boldsymbol{r})}$, and $\boldsymbol{B}$ is the external magnetic field.

[16] a two-component vector

2.12. Magnetocrystalline anisotropy calculation

Because the Hamiltonian in Eq. (2.27) does not depend on the spin, the magnetic moments have no preferential direction–they have no anisotropy [46]. To observe magnetic anisotropy, it is necessary to include relativistic effects, namely the spin-orbit coupling, illustrated by a semi-classical model in Sec. 1.5.

Within the density functional theory, magnetocrystalline anisotropy energy E_{MCA} can be calculated by three methods [35]: full relativistic total energy calculation [104], force theorem [105, 106], or the torque method [107].

The force theorem method is used in this work. By the argument that E_{SOC} is small ($\approx$ 1 meV) compared with the crystal field energy ($\approx$ 1 eV) [32], the spin-orbit coupling is treated as a perturbation. The E_{MCA} calculation consists of two steps:

1. A spin-polarized calculation is performed to obtain the ground-state density self-consistently.

2. With the spin-orbit coupling included and keeping the electron density from the previous step, the total energy for different magnetization directions is calculated.

Since E_{MCA} is so small, special care must be taken that the total energies are calculated precisely, namely that a sufficient number of k-points and sufficiently high plane-wave cutoff energy is used.

2.13. Vienna *Ab Initio* Simulation Package (VASP)

The Vienna *Ab Initio* Simulation Package (VASP) [108–110] is a complex commercial package for ab initio simulations. It is written in Fortran 90 and uses MPI [111, 112] to enable massively parallel computing on clusters. The PAW method is employed for accurate calculations with a small enough basis. It has good scalability for large systems (calculations for up to $\sim$ 4000 valence electrons), and there are routines that automatically calculate the symmetry of the problem, to simplify the computation. Throughout this work, VASP version 5.4.4. is used for self-consistent collinear calculations and version 5.4.1. for noncollinear non-selfconsistent calculations.

In the following, the general inputs and outputs of a VASP calculation are outlined. They are logically grouped into several text files.

Input files

Four input files are always needed in a VASP calculation:

1. POSCAR

In the POSCAR text file, we define the size and shape of the unit cell, along with the positions and types of atoms it contains. Periodic boundary conditions are usually applied in all directions, so the unit cell virtually repeats and fills the whole space.

2. INCAR

The INCAR text file contains most of the calculation settings, namely the type of calculation and the specific algorithms used, the size of plane-wave basis and precision of convergence criteria, whether magnetism should be included, and what are the starting magnetic moments for each atom, and so on. We can also define how to parallelize the computation and how strongly the symmetry conditions should be enforced. Most parameters have reasonable default values and do not have to be modified, depending on the requirements.

3. KPOINTS

The periodic boundary conditions make VASP ideal for solid-state materials calculations, where the Bloch theorem and notion of the Brillouin zone play a central role [39]. The electronic ground state should be calculated for all the (infinite number of) k-points inside the Brillouin zone and then integrated. In practice, the Brillouin zone is sampled by some limited number of k-points and then summed. The type of sampling and the number of k-points (density of the k-point mesh) is specified in the KPOINTS file.

4. POTCAR

POTCAR contains the pseudopotentials for each atomic element used in POSCAR. The pseudopotentials are created by the developers and copy-pasted into POTCAR, depending on which ones are currently needed.

Output files

The output of the calculation is naturally the ground-state density, given in the CHGCAR file, along with the wave functions given in WAVECAR. However, most of the relevant parameters are given in OUTCAR.

OUTCAR

OUTCAR contains information about the calculation progress and a plethora of important output parameters. These are the symmetry of the problem, total energy, the energy eigenvalues at all sampled k-points, relaxed atomic positions (if atomic relaxation was performed), forces on atoms, magnetic moments (including the orbital moments), and far more.

PROCAR

In PROCAR, for each particular band at each particular k-point, the *character* of this band is provided as a set of complex numbers for all the nuclei, orbitals, and spins, where the complex number is the projection coefficient of the particular wavefunction with a given spin onto a given spherical harmonic (orbital type) centered at the given nucleus.

DOSCAR

DOSCAR contains the *density of states* (DOS) resolved in spin, orbital type, and nucleus site.

3. Magnetic anisotropy of bcc Fe, Co, and Ni/MgO ultrathin films

The manyfold cutting edge applications of MgO-based magnetic tunnel junctions have been described in the Introduction. In this thesis, we focus on their applications in the spin-transfer torque magnetic random access memory (STT-MRAM). Specifically, we aim to increase their perpendicular magnetic anisotropy (PMA) to enable further downsize scaling of STT-MRAM memory bits (Sec. 1.6). The ferromagnetic layers in MgO-based MTJs are usually composed of the 3*d* transition elements Fe and Co in their body-centered cubic (bcc) crystal structure. In this chapter, we start by investigating the PMA of ultrathin films of bcc Fe, Co, and Ni on MgO by ab initio calculations.

3.1. Magnetocrystalline anisotropy calculation procedure

The density functional theory (DFT) calculations of magnetocrystalline anisotropy are performed using the *Vienna Ab initio Simulation Package* (VASP) [109, 110] (Sec. 2.13).

The Generalized gradient approximation (GGA) exchange-correlation functional [113] (Sec. 2.9) is used as implemented by Perdew, Burke, and Ernzerhof [87]. The k-point mesh of 25 x 25 x 1 points and a plane wave cut-off energy of 520 eV (`ENCUT = 520`) has proven to give sufficient accuracy, as discussed in Sec. 3.2. We follow the force-theorem method [105, 106], already introduced in Sec. 2.12.

The whole calculation procedure is described in detail in Ref. [114, 115] and it consists of four steps:

1. **Relaxation**. First, the unit cell shape, volume, and atomic positions are adjusted to minimize the interatomic forces[1] below 0.001 eV/Å (`EDIFFG = -0.001`).

2. A **self-consistent optimization** of the ground-state electronic structure is performed, until the total energy variation drops below 10^{-7} eV (`EDIFF = 1e-7`).

3. **Spin-orbit interaction is included** (`LSOC=.TRUE.`) and the total energy of the system is calculated non-self-consistently, with the electronic charge density from the previous step (`ICHARG=11`); the magnetization is out-of-plane (`SAXIS = 0 0 1`).

4. Same as step 3, but with magnetization in-plane (`SAXIS = 1 0 0`).

[1] obtained from the Hellmann-Feynman theorem [116, 117]

The magnetocrystalline energy E_{MCA} is then defined as the total energy difference for magnetization in-plane $\boldsymbol{m}_{||} = (1, 0, 0)$ and out-of-plane $\boldsymbol{m}_{\perp} = (0, 0, 1)$

$$E_{\mathrm{MCA}} = E(\boldsymbol{m}_{||}) - E(\boldsymbol{m}_{\perp})\,. \tag{3.1}$$

3.2. Convergence tests

As mentioned in Sec. 2.12, E_{MCA} is a very small energy difference ($\sim$ 1 meV), compared with the total energy ($\sim$ 100 eV). In our case, it makes up for a tiny $\sim$ 0.001% of the total energy, and special care must be taken to perform calculations that are sufficiently accurate. Therefore, we first carry out several *convergence tests*.

The k-point mesh

The k-point mesh determines how densely the Brillouin zone should be sampled. In Fig. 3.1(b), a two-dimensional Brillouin zone with 4x4 k-point mesh is sketched[2]. Denser mesh means higher precision but longer computation time. Before any calculation, it is hence important to determine the minimal k-point mesh density, which still ensures the required precision. We perform a k-point convergence test on a structure with a 5-monolayer (ML) film of bcc Ni sandwiched between 5 MLs of MgO.

In Fig. 3.1(a), we plot E_{MCA} vs. $n_{\mathrm{k,lateral}}$, where the k-point mesh is $n_{\mathrm{k,lateral}} \times n_{\mathrm{k,lateral}} \times 3$ k-points. The data is fitted by an exponential to obtain the asymptotic value. For most of the calculations, though, 1 k-point in the z direction is enough and a mesh of $25 \times 25 \times 1$ k-points has proven to give a reasonable trade-off between accuracy and computation time.

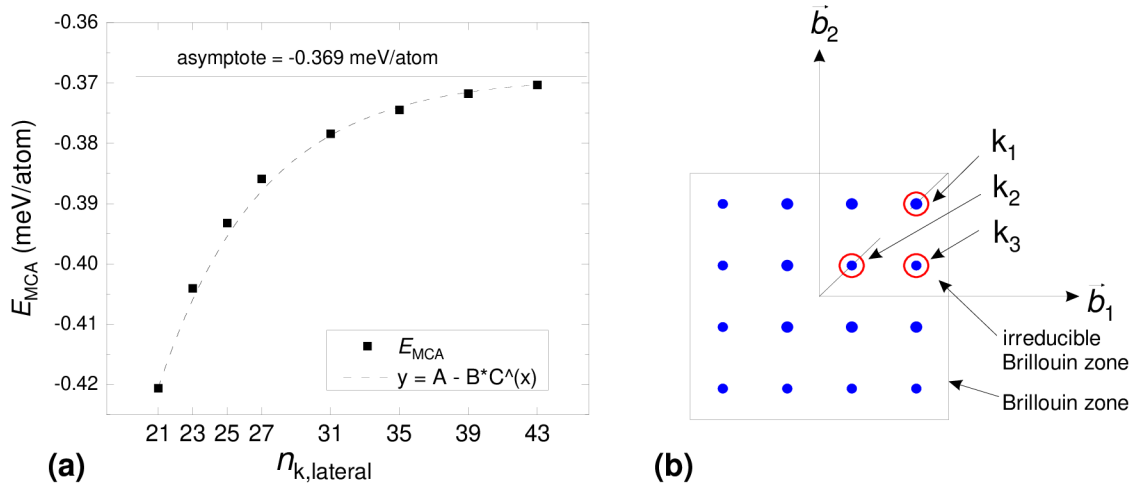

Figure 3.1: (a) K-points convergence test performed on bcc Ni(5ML)/MgO(5ML) and a $n_{\mathrm{k,lateral}} \times n_{\mathrm{k,lateral}} \times 3$ k-point mesh. (b) A 2D Brillouin zone with a small, illustrative 4x4 kpoint mesh. Only 3 out of the 16 points are unique. The *irreducible Brillouin zone* thus covers only 1/8 of the whole Brillouin zone. From [118].

[2]Note that due to symmetry, only 3 k-points are unique, forming the much smaller *irreducible* Brillouin zone. This reduction of k-points by symmetry considerations greatly simplifies the calculation in steps 1 and 2 in Sec. 3.1. However, for Steps 3 and 4, where the spin-orbit coupling is included, the symmetry is broken and should be switched off (`ISYM = -1`).

The plane-wave energy cut-off

To make the plane-wave basis finite, one needs to set the highest spatial frequency, which still needs to be included in the plane-wave basis to accurately describe the charge density oscillations with sufficient resolution. In VASP, instead of the spatial frequency cut-off G_{cut}, we set the wave's corresponding cut-off kinetic energy

$$E_{\text{cut}} = \frac{\hbar^2}{2m_e} G_{\text{cut}}^2 \tag{3.2}$$

defined by the `ENCUT` parameter in `INCAR`. Default values are available in VASP for each element. We use $E_{\text{cut}} = 520$ eV. The change in E_{MCA} following the change in E_{cut} from 500 eV to 550 eV is[3] only 2^{-4} meV.

Note that increasing the MgO thickness from 5ML to 7ML has only a small effect on E_{MCA}, below 0.01 meV.

3.3. Body-centered cubic (bcc) lattice of Co and Ni

The natural lattice-type for bulk Fe is indeed the body-centered cubic (bcc), but for Co, it is hexagonal close-packed (hcp), and for Ni, it is face-centered cubic (fcc). That is why, with no MgO present, thin slabs of Co and Ni prefer the fcc structure over bcc: if we impose the bcc structure on a few-monolayer-thick Co or Ni slab interfaced with vacuum and let it relax, the lattice expands vertically by a factor of $\sqrt{2}$, as shown in Fig. 3.2. This corresponds to a bcc→fcc transformation; the fcc lattice is clearly apparent if the relaxed structure is rotated by 45° (see Fig. 3.2). The Fe slabs always stay in the bcc form.

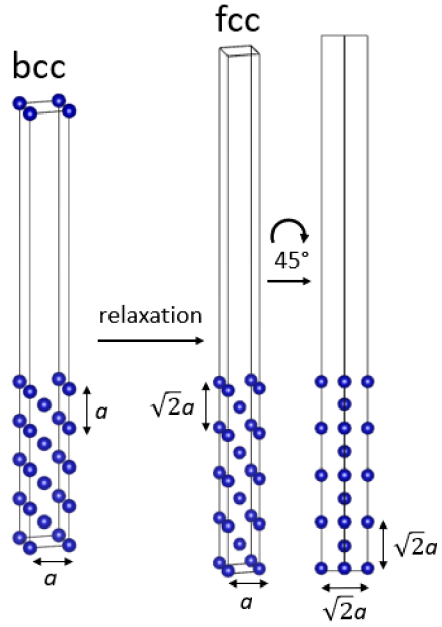

Figure 3.2: A Co or Ni slab (thin film interfaced with vacuum) relaxes from the initial bcc form to fcc by a vertical expansion. In Fe, whose natural bulk lattice type is bcc, we do not observe this transformation.

[3] for the Ni/MgO test system and 25×25×3 k-points

On the contrary, if the slabs are interfaced with MgO, the relaxation *compresses* the lattice slightly in the vertical direction, making the lattice strained. Hence, (a strained) bcc lattice of Co and Ni is *stabilized by the MgO barrier*.

3.4. Test calculations: reproducing published results

To check that the calculation as described above is set up correctly, we try to reproduce some well-known published results.

First, the results of hybridization between the Fe d orbitals and the O p_z orbital at the Fe/MgO interface are studied. This hybridization plays a central role in the large out-of-plane interfacial anisotropy in Fe/MgO MTJs[4]. Hence, we follow the work of Yang *et al.* [114] and plot the energy levels of the interfacial Fe d-orbitals and the interfacial O p_z orbital in Fe(5ML)/MgO(5ML). Our results are shown in Fig. 3.3, side by side with the results from Yang *et al.* [114]. The energy level positions correspond well, and the hybridization of the O p_z orbital with Fe d_{z^2} orbital is apparent, as explained in the caption of Fig. 3.3.

Second, we perform the E_{MCA} calculation for Fe/MgO with Fe thickness from 5 to 15 MLs. For all the films, we determine the contribution from each of the layers and compare with Ref. [119]. As shown in Fig. 3.4, our results again coincide very well with the published ones.

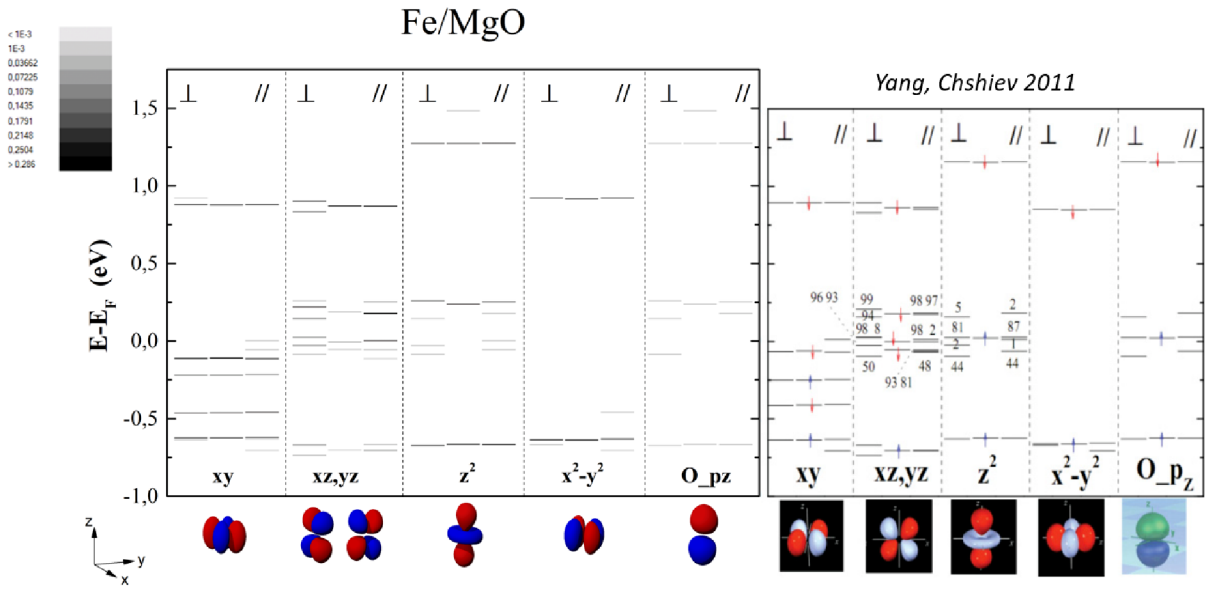

Figure 3.3: The energy levels of the five d-orbitals (xy, xz, yz, z^2, and x^2-y^2) at the interfacial Fe and the p_z orbital of the interfacial O (O_pz) in Fe/MgO are shown for three cases: without spin-orbit coupling (middle column of energy levels), with SOC plus magnetization out-of-plane (⊥; left column), with SOC plus magnetization in-plane (//; right column). With SOC included (left and right column), additional energy levels appear in the oxygen p_z orbital, corresponding to certain Fe d_{z^2}. This signifies the presence of hybridization between the two orbitals, which is the main cause of interfacial PMA in Fe/MgO [114].

[4]The interfacial anisotropy between Fe and O makes it possible to fabricate perpendicular MgO-based MTJs, very important for MRAM applications [1].

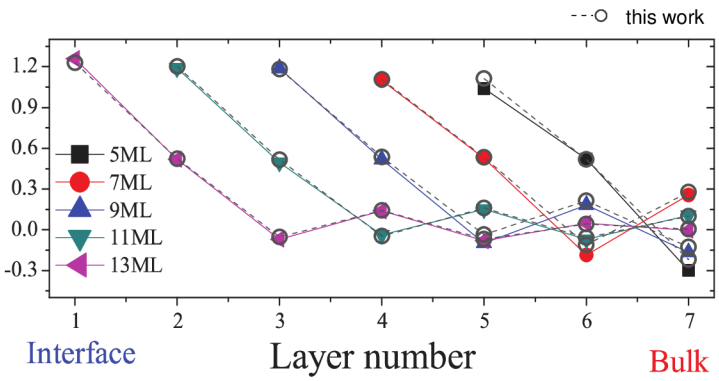

Figure 3.4: Layer-resolved E_{MCA} for Fe/MgO of different Fe thicknesses. The grey empty circles (calculated in this work) correspond well to the literature results (the colored symbols, calculated in Ref. [119]).

3.5. Varying the metal thickness

After validating the accuracy of the calculation procedure, we continue with a series of calculations for bcc (001) Fe, Co, and Ni on MgO as a function of metal thickness. In Fig. 3.5, we plot their E_{MCA}, the in-plane lattice parameter a, and the average atomic magnetic moment μ.

Magnetocrystalline anisotropy

From Fig. 3.5(a), it is clear that for Fe, the E_{MCA} stays almost constant with thickness. This is well known [119]. For Co, on the other hand, there is a steady increase. For Ni, the behavior seems oscillating.

According to Eq. (1.3), constant variance with thickness points to interfacial anisotropy, while linear increase points to bulk anisotropy [also indicated in the inset of Fig. 3.5(a)]. We confirm the origin of these distinct trends by plotting the contribution to E_{MCA} from each of the metallic layers separately in Fig. 3.5(b).

For **Fe**, the main contribution to E_{MCA} comes from the first two layers at the MgO interface [114, 119, 120]. Increasing the thickness does not affect the electronic properties of the interfacial layers in a significant way [119] (see Fig. A.1 in Appendix A). The contribution of the bulk layers is almost zero. When increasing the Fe thickness, only bulk-like layers are added. Hence the E_{MCA} does not change with thickness.

Interestingly, for **Co**, all the bulk layers seem to contribute with a significant positive value [120], evident from Fig. 3.5(b). This is why the E_{MCA} in Fig. 3.5(a) grows monotonically: by increasing the thickness, more bulk-like layers are added and each of them gives a contribution of about 0.5 mJ/m^2.

In **Ni**, the influence of the interface manifests itself as deep as 6 ML [120]. The two interfacial layers contribute negatively to E_{MCA}. This is the reason for the in-plane anisotropy in the 5-ML structure in Fig. 3.5(a). Although the deeper bulk layers contribute positively, the E_{MCA} does not grow monotonically, as one could expect, because the interfacial contributions in Ni do change upon thickness increase, unlike in Fe or Co (Fig. A.1 in Appendix A).

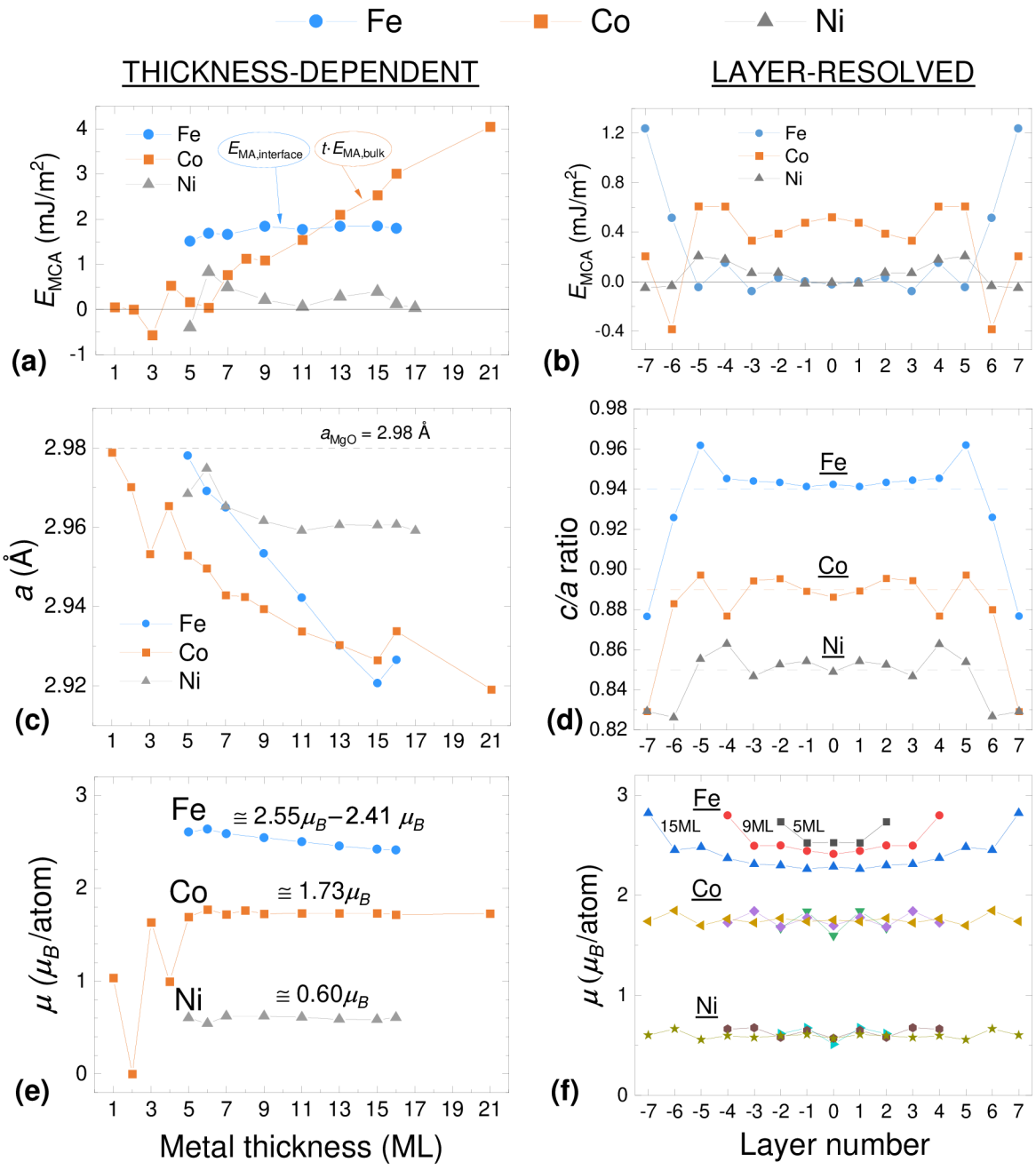

Figure 3.5: (a) The magnetocrystalline anisotropy for structures comprising bcc Fe, Co, and Ni on MgO as a function of metal thickness. Constant variance for Fe signifies presence of interfacial anisotropy; linear increase for Co signifies bulk anisotropy. This is confirmed by the layer-resolved values in metal(15ML)|MgO structures in part (b). (c) In-plane lattice parameter. With increasing metal thickness, it relaxes from the MgO bulk value towards the smaller Fe, Co, and Ni bulk values. The decrease is least prominent for Ni, which mainly relaxes via vertical lattice parameter c: its c/a ratio in part (d) deviates most from the equilibrium $c/a = 1$. (The c/a ratio in bulk layers of Fe, Co, and Ni is 0.94, 0.89, and 0.85, respectively.) The layer-resolved c/a values plotted for the 15ML-thick structure in part (d) are very similar across all thicknesses, see Fig. A.2 in Appendix A. (e) The average atomic magnetic moment is almost constant for Co and Ni, but decreases for Fe. (f) Only in Fe are the interfacial magnetic moments enhanced.

Lattice parameter and strain

In Fig. 3.5(c), the lattice parameter for the thinnest metal thicknesses is very close to that of bulk MgO: $a_{\mathrm{MgO}} = 2.98$ Å [121]. The 5ML-thick MgO imposes this lattice parameter upon the thin metals. For thicker metal layers, the a parameter starts to decrease (it *relaxes*) towards the bulk values of the respective bcc metals: $a_{\mathrm{Fe}} = 2.86$ Å [122], $a_{\mathrm{Co}} = = 2.81$ Å [123], $a_{\mathrm{Ni}} = 2.79$ Å [this work].

The a relaxation is most prominent for Fe, less so for Co, and even less for Ni. This might seem surprising: from the lattice parameters given above, the lattice *mismatch* is biggest for Ni, lower for Co, and lowest for Fe. We would hence expect the steepest decrease of a in Fig. 3.5(c) for Ni. However, Ni relaxes mainly via the *vertical* lattice parameter c.

In other words, the c/a lattice parameter ratio for Ni most deviates from the equillibrium value $c/a = 1$. This is clear from Fig. 3.5(d): the typical relaxed c/a ratios we found within the bulk-like layers of Fe, Co, and Ni on MgO are 0.94, 0.89, and 0.85, respectively. (We devote the next Sec. 3.6 to the effect of strain on the E_{MCA} in purely bulk bcc Fe, Co, and Ni.)

Atomic magnetic moment

The average magnetic moment per atom [Fig. 3.5(e)] stays *almost constant* for the larger thicknesses of Co and Ni. (For the thinnest Co, there are strong variances due to the extreme strains in these ultrathin structures.) For Fe, however, the average atomic magnetic moment *decreases* with thickness. This has been observed both theoretically and experimentally [124, 125]. Also, there is an interfacial magnetic moment enhancement in Fe/MgO, see Fig. 3.5(f). Its consequences for magnetic tunnel junctions were discussed in Ref. [126].

3.6. Strained bulk bcc Fe, Co, and Ni

In order to understand what is the cause of the large bulk PMA in bcc Co in Fig. 3.5(b), based on Fig. 3.5(d), we make a hypothesis that this large PMA is strain-induced.

To determine the effect of strain on bulk bcc Fe, Co, and Ni, we perform a series of anisotropy energy calculations of a simple bcc unit cell of Fe, Co, and Ni with different c/a ratios [Fig. 3.6(a)]. A k-point mesh of 19×19×19 points has proven to provide E_{MCA} with sufficient accuracy of 0.01 meV. The typical bulk strains from Fig. 3.5(d) are plotted as vertical lines. At its typical c/a ratio (0.89), there is indeed a strain-induced anisotropy of about 0.5 mJ/m^2 for bulk bcc Co in Fig. 3.6(b). This is the same value as in the bulk layers of Fe on MgO in Fig. 3.5(b).

Thereby, the hypothesis of significant strain-induced PMA in Co/MgO is supported. We have performed some additional tests, notably making the structure artificially unstrained ($c/a = 1$) and omitting the relaxation step in the calculation. The result was that the PMA in Co disappeared, as expected.

The E_{MCA} in strained bulk bcc Fe, Co, and Ni has been calculated before [127, 128], but only in the range $c/a > 1$, whereas our region of interest is $c/a < 1$ (the typical strains of metal/MgO structures). Our results correspond well to the published values for $c/a > 1$, see Fig. A.3 in Appendix A.

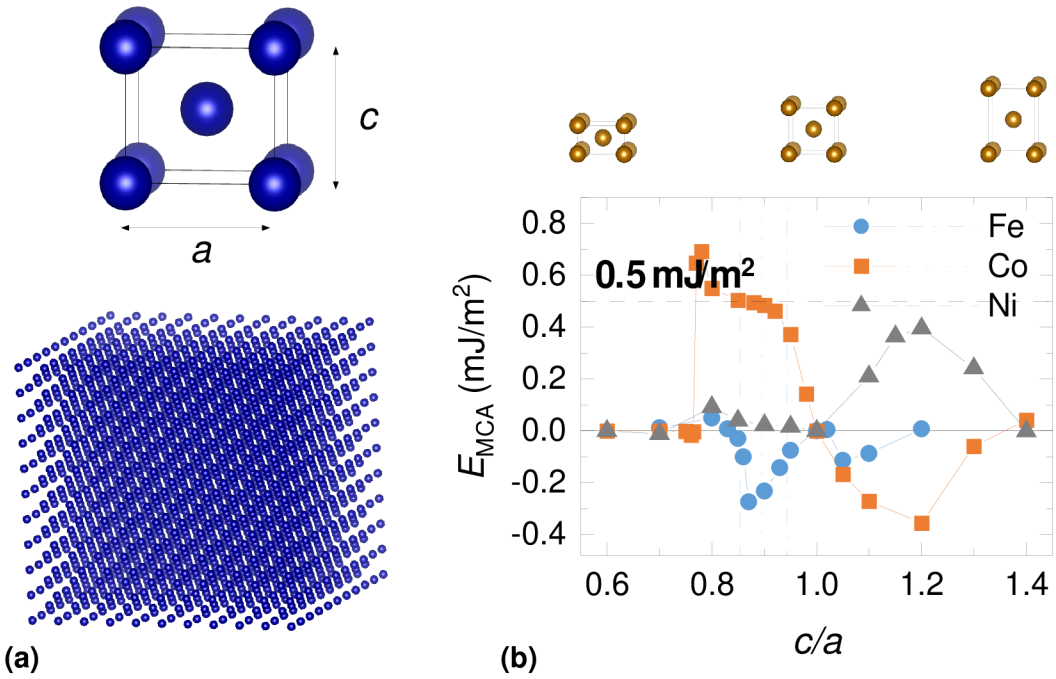

Figure 3.6: (a) A simple bcc unit cell with the vertical lattice parameter c and the latteral lattice parameter a. It serves as a model structure for evaluating the impact of strain on the PMA of Fe, Co, and Ni on MgO. (b) The E_{MCA} was calculated for different c/a ratios. Vertical lines signify the typical c/a values in bulk-like layers of bcc Fe, Co, and Ni on MgO. At the typical c/a for Co (0.89), the E_{MCA} is indeed about 0.5 mJ/m^2, same value as in Fig. 3.5(b). This supports the hypothesis that the PMA in bcc Co in Fig. 3.5(b) is strain-induced. Note that the values for $c/a > 1$ correspond reasonably well to published results [127, 128] (see Fig. A.3 in Appendix A).

4. Giant anisotropy enhancement in Fe/Co/Fe|MgO magnetic tunnel junction

In this Chapter, we exploit the results of the previous Chapter 3, namely that there is a large PMA arising at the Fe/MgO interface and a large PMA contribution coming from the Co/MgO bulk.

4.1. PMA enhancement due to E_{MCA}

We propose to enhance the PMA of a conventional Fe/MgO MTJ by replacing a few of the bulk Fe layers with Co [120]. In Fig. 4.1, this concept is demonstrated. A conventional MTJ is shown, consisting of a fixed magnetic layer, the MgO barrier, and a magnetic storage layer composed of a Fe(3 ML)/Co(10 ML)/Fe(3 ML) trilayer. The Co atoms in the middle of the structure enhance the PMA, compared with a structure with pure Fe. Following the arguments of Sec. 3.5 and Sec. 3.6, the large PMA in the bulk Co layers is induced by the epitaxial strain caused by MgO.

In Fig. 4.2(a), we plot E_{MCA} for structures with the general form Fe(n)/Co(m)/Fe(n)|MgO for different Fe and Co thicknesses n and m, respectively. The enhancement mechanism is persistent for all the cases. Note, however, how the first Co layer at the Fe/Co interface loses its positive PMA. Especially from the "$n = 4$, $m = 4$" case in Fig. 4.2(a) it

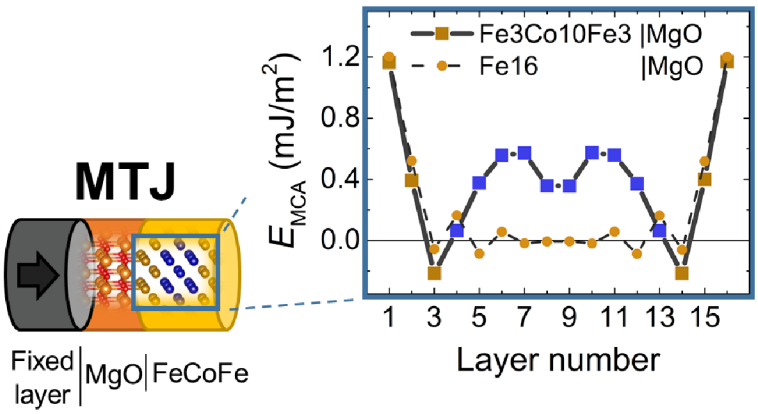

Figure 4.1: The concept of PMA enhancement in a conventional Fe/MgO MTJ by replacing a few of the bulk layers by Co. The bulk Co atoms (blue) provide large contribution to E_{MCA}. Also, they reduce the negative demagnetizing energy, as discussed in the text.

is apparent that a Co thickness of $m < 4$ monolayers might lose the enhancing property altogether.

Indeed, we find that the **condition for the enhancement to work** is to have at least two Fe monolayers ($n \geq 2$) and at least three Co monolayers ($m \geq 3$). In Fig. 4.2(b), we plot the layer-resolved E_{MCA} for this "minimal structure" Fe(2ML)/Co(3ML)/Fe(2ML)|MgO, as well as for several structures defying the $\boldsymbol{n \geq 2, m \geq 3}$ rule, which is clearly detrimental for the PMA.

While E_{MCA} shows very promising enhancement in our presented Fe(n)/Co(m)/Fe(n)|MgO magnetic tunnel junction design, so far we have not considered the important contribution of shape anisotropy.

4.2. Shape anisotropy (E_{dd}) calculation

We implement a Python code to calculate the shape anisotropy. The code first loads the (relaxed) positions and dipolar magnetic moments of all the atoms calculated by VASP. The total dipolar energy E_{dipolar} [Eq. (1.7)] is then obtained for magnetization in-plane $\boldsymbol{m}_{||} = (1, 0, 0)$ and out-of-plane $\boldsymbol{m}_{\perp} = (0, 0, 1)$. The shape anisotropy energy (dipolar demagnetizing energy) is defined as [129, 130]

$$E_{\mathrm{dd}} = E_{\mathrm{dipolar}}(\boldsymbol{m}_{||}) - E_{\mathrm{dipolar}}(\boldsymbol{m}_{\perp})\,, \tag{4.1}$$

similar to the definition of E_{MCA} [Eq. (3.1)].

Note that the unit cell in VASP is small, but due to the periodic boundary conditions, it effectively forms an infinite thin film, which is exactly the geometry we are interested in. Now, the dipole-dipole interactions should also be summed up to infinity in the two x and y in-plane directions[1]. In practice, the code performs a sum up to some finite cut-off radius r_{cut} [see the inset in Fig. 4.3(a)] for a few selected values of r_{cut} ($\sim$100 unit cells). Then we interpolate $E_{\mathrm{dd}}(r_{\mathrm{cut}})$ with the formula

$$E_{\mathrm{dd}}(r_{\mathrm{cut}}) = a\, r_{\mathrm{cut}}^{-b} + c\,. \tag{4.2}$$

This expression is justified by the fact that the dipole-dipole energy $\propto 1/r_{\mathrm{cut}}^3$ and the number of atoms of the thin infinite film $\propto r_{\mathrm{cut}}^2$ (the surface area), so overall $E_{\mathrm{dd}} \propto 1/r_{\mathrm{cut}}$ [see Fig. 4.3(a)]. Hence, we expect $b \approx 1$, which is also what we observe in fits similar to that in Fig. 4.3(a). The desired asymptotic value is clearly the c coefficient

$$E_{\mathrm{dd}}(r_{\mathrm{cut}} \to \infty) = c\,. \tag{4.3}$$

After testing the code, we arrive at the following conclusions.

1. Quite a low cut-off radius of only several tens of unit cells is enough for a precise extrapolation by Eq. (4.2). Namely in our test case, we compare the results of extrapolating $E_{\mathrm{dd}}(r_{\mathrm{cut}} \to \infty)$ from $r_{\mathrm{cut}} \in \{10, 30, 50\}$ and from $r_{\mathrm{cut}} \in \{500, 1000, 2000\}$. The difference is only 0.3% and the computation time for the first case is orders of magnitude shorter. Using this low cut-off radius, we reproduce the results from Ref. [129] with good precision ($\approx 1\%$).

[1] Note that in VASP, the periodic boundary condition is also in the z direction, perpendicular to the film. This effectively makes the structure an infinite number of parallel thin double-barrier magnetic tunnel junctions. Since the magnetic layers are separated by MgO, this is of no concern in the DFT calculation, but for the E_{dd}, implying the periodic boundary condition in z would be meaningless.

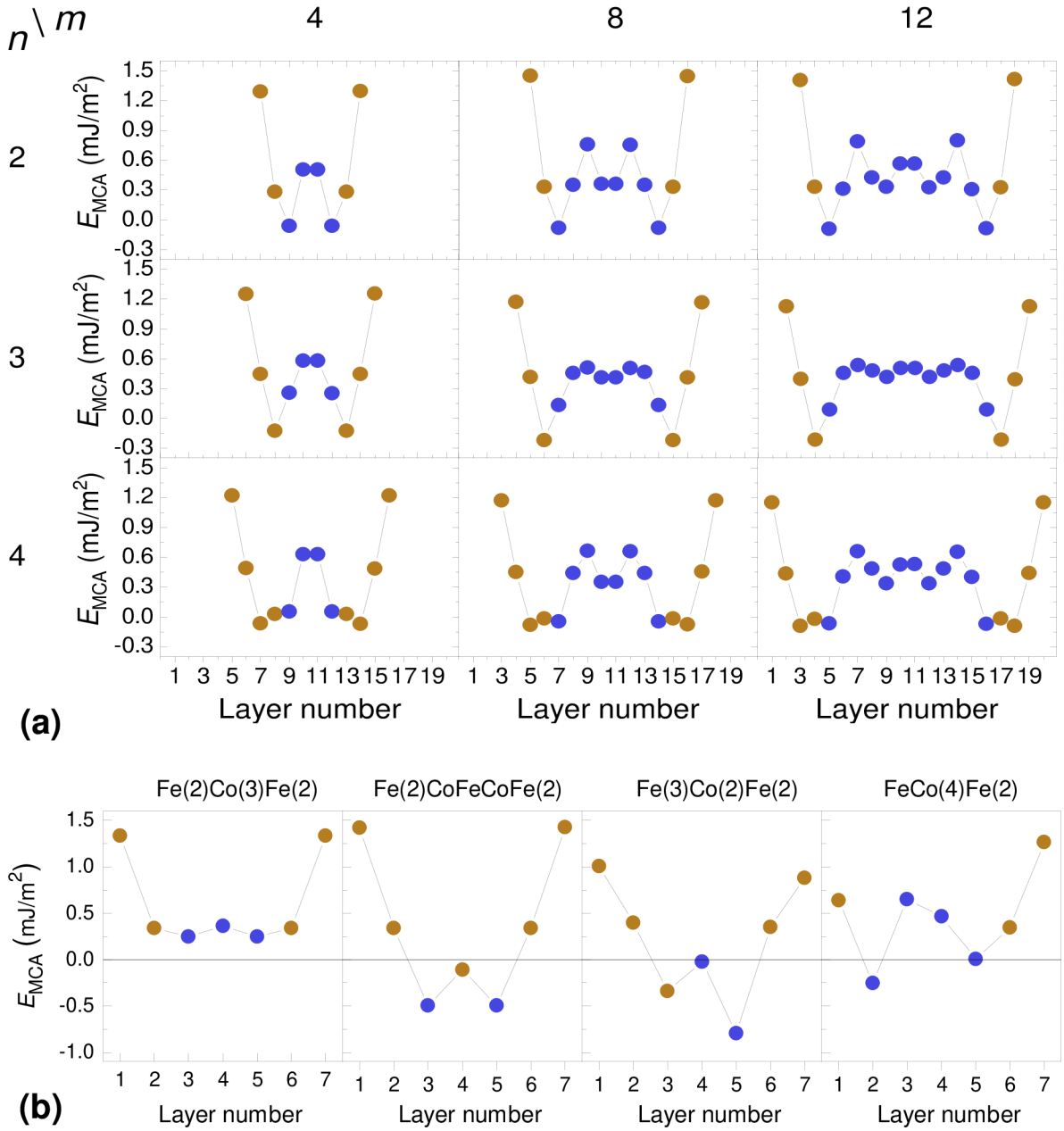

Figure 4.2: (a) Layer-resolved E_{MCA} in structures of the form Fe(n)/Co(m)/Fe(n)|MgO. Gold circles represent Fe layers and blue circles represent Co layers. The enhancement of E_{MCA} compared to a pure Fe|MgO structure is provided by the bulk Co layers, similar to Fig. 4.1 [120]. The Fe/Co interface is detrimental to the bulk Co PMA of the Co layer closest to Fe. (b) We find that at least 2 Fe layers and 3 Co layers are needed for the enhancement. This "minimal" structure is on the very left. The other structures defying this condition do not exhibit the large enhancement. © 2021 American Physical Society [120].

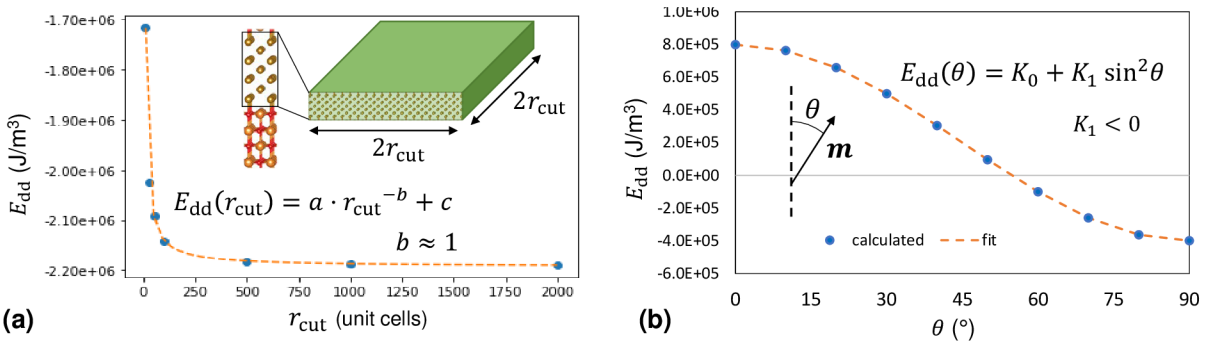

Figure 4.3: (a) The dipolar demagnetizing energy E_{dd} for a Fe(7ML)/MgO finite thin rectangular film with a diameter of $2r_{cut}$ unit cells. The scaling is close to $E_{dd} \propto 1/r_{cut}$, i.e., $E_{dd}(r_{cut}) = a\, r_{cut}^{-b} + c$ with $b \approx 1$. (b) The dipolar demagnetizing energy as a function of the magnetization angle θ from the perpendicular direction. The $E_{dd}(\theta)$ has the form of uniaxial anisotropy [Eq. (1.2)]. Tested on Fe(7ML)/MgO.

2. The calculation values are very similar to the simple formula Eq. (1.6) for thin magnetic films [30]

$$E_{\text{demag, thin-film}} = -\frac{\mu_0}{2} M_s^2 \,, \tag{4.4}$$

where M_s is the *average* magnetization over the whole unit cell. Indeed, Eq. (4.4) underestimates the shape anisotropy only by a few percent, as shown in Tab. 4.1.

3. The angular dependence of E_{dd} is uniaxial [Eq. (1.2)], which is apparent from Fig. 4.3(b).

Table 4.1: Comparing E_{dd} calculated by the average demagnetizing field [Eq. (4.4)] and the dipole sum [Eq. (1.7)] in a few selected structures. The underestimate of $E_{\text{demag, thin-film}}$ compared to E_{dd} is also given.

	$E_{\text{demag, thin-film}}$ (MJ/m³)	E_{dd} (MJ/m³)	underestimate (%)
Fe(5ML)|MgO	-2.02	-2.09	3.4
Fe(7ML)|MgO	-2.17	-2.19	1.1
Fe(15ML)|MgO	-2.11	-2.15	1.5
Fe(2ML)Co(3ML)Fe(2ML)|MgO	-1.72	-1.78	3.1

4.3. PMA enhancement due to E_{MCA} and E_{dd}

We have thus two major contributions to the *effective perpendicular anisotropy*

$$\text{PMA} = E_{MCA} + E_{dd} \,. \tag{4.5}$$

By replacing the bulk-like layers in Fe/MgO, we obtained large enhancement due to E_{MCA} [Fig. 4.1]. In addition, there is **enhancement also due to E_{dd}**. This is clear from the following argument, which we make for the simplified expression Eq. (4.4), but it can be made very similarly for the more accurate Eq. (1.7) [along with Eq. (4.1)]: since E_{dd} is

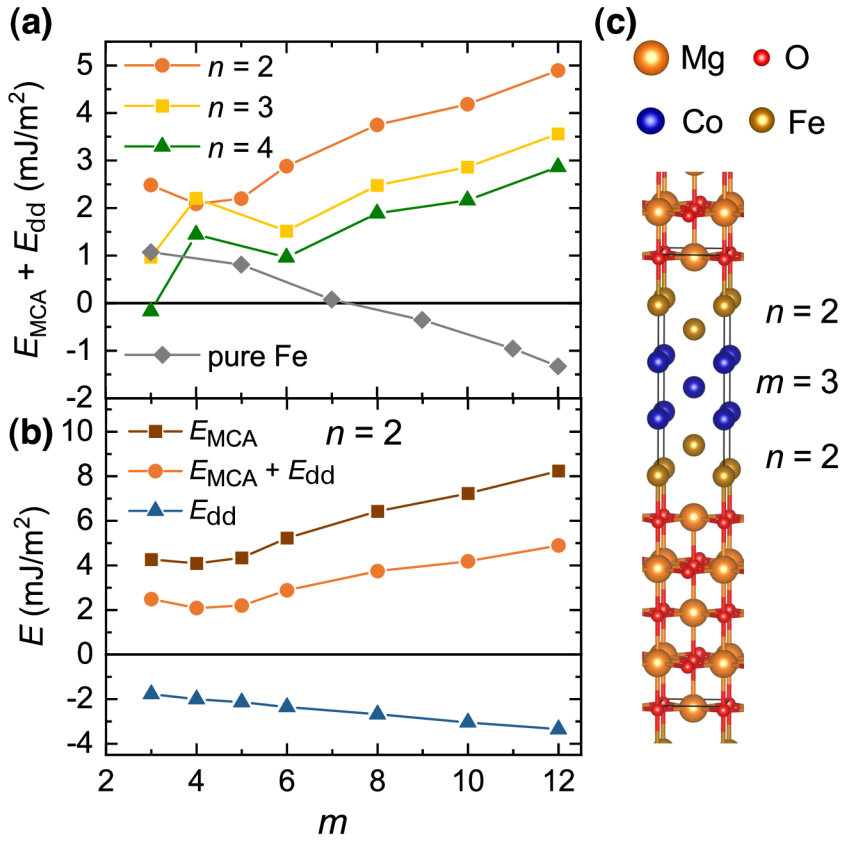

Figure 4.4: (a) Effective PMA (E_{MCA}+E_{dd}) in MgO|Fe(n)Co(m)Fe(n)|MgO as a function of number of monolayers n, m. There is no perpendicular to in-plane magnetic anisotropy switching compared to pure MgO|Fe|MgO (grey diamonds; its thickness is m+4 ML, the same as the overall thickness for n=2) [120]. (b) E_{MCA}, E_{dd}, and the effective PMA (E_{MCA}+E_{dd}) for n=2. The effective PMA increases with the Co thickness [120]. (c) Supercell of the MgO|Fe(2)Co(3)Fe(2)|MgO with periodic boundary conditions applied in all directions [120]. Produced by VESTA [131]. © 2021 American Physical Society [120].

negative, the (positive) perpendicular anisotropy energy is increased when the magnitude of E_{dd} is decreased. Since the magnetic moment of Co [$\approx 1.73\mu_B$] is lower than that of Fe [$\approx 2.5\mu_B$; Fig. 3.5(e)], E_{dd} is weaker and the effective perpendicular anisotropy is enhanced even stronger.

In Fig. 4.4(a), we plot the effective PMA $= E_{\mathrm{MCA}} + E_{\mathrm{dd}}$ as a function of Fe and Co thicknesses n and m. Usually, above certain film thickness, the demagnetizing energy dominates, making the effective anisotropy negative (in-plane). This is clear from the pure Fe|MgO case (grey line). In contrast, the effective PMA in our Fe(n)/Co(m)/Fe(n)|MgO does not become negative; due to the two enhancement mechanisms, it grows steadily, just as in the pure Co/MgO case [Fig. 3.5(a)]. The variation of E_{MCA} and E_{dd} separately (for $n = 2$) is shown in Fig. 4.4(b). The storage layer design with enhanced anisotropy is depicted in Fig. 4.4(c).

4.4. Decrease of PMA with Fe/Co interdiffusion

In the real-life fabricated structures, there will be some interdiffusion between the neighboring layers. The sharpness of the Fe/Co interface is, therefore, an important factor to

consider [120]. From the simulations, it follows that any interdiffusion is fatal for the PMA when the Fe or Co thickness is less than 2 ML or 3 ML, respectively [n<2 or m<3; Fig. 4.2(b)]. Robustness can be achieved at larger Fe and Co thicknesses. In Fig. 4.5, one may see the effective PMA in the Fe(2)Co(3)Fe(2) and Fe(3)Co(4)Fe(3) structures with 0.5-ML (50%) interdiffusion and a 1-ML interdiffusion (the interface layers are completely swapped). The drop in the effective PMA in Fe(3)Co(4)Fe(3) is only 22% at 0.5-ML interdiffusion, compared to a drop of 73% for Fe(2)Co(3)Fe(2). This robustness against surface roughness is to be expected in the thicker structures in general [120].

Larger Co thickness is favorable as it increases the PMA [Fig. 4.4(a)], but thicker bcc Co will probably be harder to fabricate [132].

On the other hand, larger Fe thickness provides robustness against interdiffusion and might stabilize the bcc Co[2], but the PMA decreases [Fig. 4.4(a)].

The goal is therefore to maximize the Co thickness as long as its structure stays stable and to minimize the Fe thickness as long as the robustness against interdiffusion is sufficient. Looking at Fig. 4.4(a) and considering all the aforementioned aspects, the MgO|Fe(3ML)Co(4ML)Fe(3ML)|MgO seems like a promising candidate as a storage layer for STT-MRAM cells with highly improved thermal stability compared to conventional STT-MRAM [120].

Indeed, when the storage layer is sandwiched between two MgO layers, the anisotropy per unit area is of the order of 2 mJ/m^2 from the interfacial contribution minus approximately 1.2 mJ/m^2 from demagnetizing energy (dependent on the chosen storage layer thickness), yielding a net effective PMA per unit area approximately 0.8 mJ/m^2 [120, 133]. In comparison, the net anisotropy per unit area in the proposed structure is approximately 2.2 mJ/m^2, being almost 3 times larger. This means that for the same thermal stability factor [Sec. 1.6], the cell area could be reduced by a factor of 3 compared to conventional MRAM [1, 120, 134].

4.5. Fabrication of the metastable bcc Co

Although the natural form of Co is hcp, the metastable bcc Co phase can be grown at room temperature [120, 135–137]. It has been successfully grown on top of Fe with thickness up to 15 ML [138], with well-defined interfaces and no visible interdiffusion. The observed strain of 10% in bcc Co|MgO is considerable but still within the limit of what is experimentally realizable [139]. Indeed, Yuasa et al. [132] fabricated bcc Co(4ML)|MgO(10ML)|Co(4ML) MTJ and measured a record-holding TMR of 410% at room temperature. As shown in Sec. 3.3, from our structural relaxation simulations, it follows that the bcc Co is preserved on top of MgO while it transforms into the fcc phase when surrounded by vacuum. Therefore, the bcc phase will probably be most stable if the device is used as a double-barrier MTJ. This also provides higher PMA from the interfacial Fe, due to the presence of two interfaces [120].

4.6. Tunneling magnetoresistance

Since we are interested in implementing this proposed storage layer in a full MTJ stack, we investigate its expected TMR amplitude [120]. A large TMR of 410% at room temperature

[2] it is generally easier to grow bcc Co on Fe than on MgO

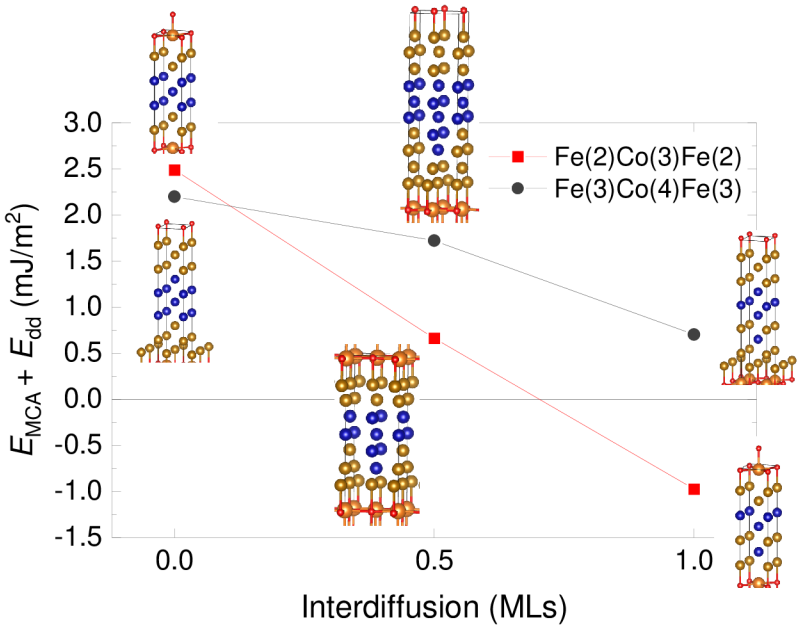

Figure 4.5: The effect of interdiffusion on the effective PMA in two selected structures. For the (minimal) Fe(2)Co(3)Fe(2) structure, there is a significant PMA decrease of 73% at 0.5-ML atomic intermixing. For the thicker Fe(3)Co(4)Fe(3), the PMA is reduced only by 22%, demonstrating the robustness against interfacial roughness. We expect this robustness in the thicker structures in general. © 2021 American Physical Society [120].

has been observed previously in pure bcc Co|MgO|Co MTJs [132]. In addition, Co in combination with Fe is often used for its record-holding TMR values. Therefore, we expect the high TMR to be present also in the proposed Fe|MgO MTJs with the inserted Co bulk layer. We estimate the TMR from the Julliere formula [3]

$$\mathrm{TMR} = \frac{G_{\mathrm{AP}} - G_{\mathrm{P}}}{G_{\mathrm{AP}}} = \frac{2P^2}{1 - P^2}\,, \tag{4.6}$$

where G_{AP} and G_{P} are the device conductivity with the two magnetization layers antiparallel and parallel, respectively, and the *spin polarization*

$$P = \frac{\mathcal{D}^{\uparrow}(E_{\mathrm{F}}) - \mathcal{D}^{\downarrow}(E_{\mathrm{F}})}{\mathcal{D}^{\uparrow}(E_{\mathrm{F}}) + \mathcal{D}^{\downarrow}(E_{\mathrm{F}})}\,, \tag{4.7}$$

where $\mathcal{D}^{\sigma}(E_{\mathrm{F}})$ is the density of states for spin $\sigma \in \{\uparrow, \downarrow\}$ at the Fermi energy E_{F}. Note that only the Δ_1 orbitals (s, p_z, and d_{z^2}) contribute to the tunneling in crystalline MgO [15]. Therefore, we account only for these states in $\mathcal{D}$. Also, it is best to take $\mathcal{D}$ of the interfacial oxygen [140]. The estimated values are very high, around 300%.

5. Second order perturbation theory calculations of E_{MCA}

The magnetocrystalline anisotropy arises due to spin-orbit coupling, as discussed in Chapter 1. The strength of the SOC is proportional to the magnitude of the spin-orbit coupling constant ξ from Eq. (1.8), which is in the order of several 10 meV [32]. This is much smaller than the width of the $3d$ band, relevant for Fe, Co, and Ni. Hence, because ξ is small, the SOC can be considered as a perturbation. E_{MCA} is then calculated within the second-order perturbation theory (PT2) framework, directly from (A) the density of states or (B) the band structure. Both the DOS and the band structure are obtained by a DFT calculation without SOC. This treatment then allows us to link the changes in E_{MCA} directly to changes in the electronic structure [120].

5.1. Bruno's theory

The PT2 approach to E_{MCA} has been developed by Bruno in 1989 [141]. The resulting formulas are complicated, as elaborated further below, but he arrived at a simple, elegant conclusion[1]: the magnetocrystalline anisotropy energy is proportional to the anisotropy of the orbital magnetic moment [1]

$$E_{\mathrm{MCA}} = \xi \frac{\Delta\mu}{4\mu_B}, \tag{5.1}$$

where ξ is the spin-orbit coupling constant and $\Delta\mu = \mu_\perp - \mu_{||}$ is the difference between the orbital magnetic moment μ with magnetization out-of-plane and in-plane. If the orbital magnetic moment prefers to lie out-of-plane, the spin magnetic moment will follow, as implied by Eq. (1.8). This creates a preference direction (anisotropy) for the spin, hence also for the magnetization[2], to lie out-of-plane.

The relatively good validity of the model, especially for bcc Fe and bcc Co on MgO, is demonstrated in Fig. 5.1.

5.2. Density of states (DOS)-based E_{MCA} calculation

We can imagine that electrons get excited from filled to empty states and these excitations contribute to E_{MCA}, depending on the spin and orbital character of the filled and empty states in question. These excitations do not happen in reality; they are only a physical

[1] valid within the perturbation approach

[2] Magnetization in $3d$ metals is mainly due to the spin magnetic moment, as the orbital angular momentum is *quenched* [31].

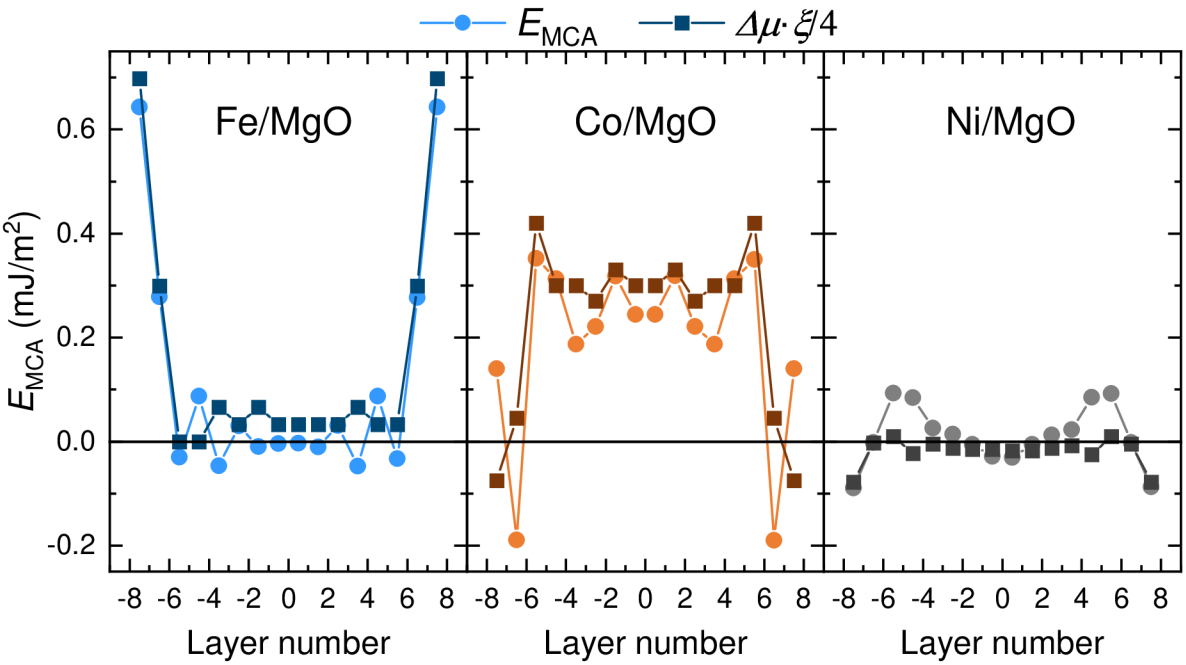

Figure 5.1: Layer-resolved E_{MCA} and $\Delta\mu$ for the *metal*(16 ML)|MgO. For Fe and Co, the E_{MCA} and $\Delta\mu$ are very well proportional, supporting the validity of Bruno's model [Eq. (5.1)]. However, the spin-orbit coupling constants used here for Eq. (5.1) are $\xi_{\mathrm{Fe}} =$ $= 133$ meV, $\xi_{\mathrm{Co}} = 60$ meV, $\xi_{\mathrm{Ni}} = 10$ meV. They are somewhat different from the values from Ref. [142] $\xi_{\mathrm{Fe}} = 68$ meV, $\xi_{\mathrm{Co}} = 84$ meV, $\xi_{\mathrm{Ni}} = 109$ meV.

picture of the equations resulting from PT2. Therefore, they are called *virtual excitations*. There are virtual excitations where the spin is conserved ($\uparrow\Rightarrow\uparrow$ and $\downarrow\Rightarrow\downarrow$) and there are spin-flip excitations ($\uparrow\Rightarrow\downarrow$ and $\downarrow\Rightarrow\uparrow$). The E_{MCA} can be written as the sum of these four terms [143]

$$E_{\mathrm{MCA}} = \Delta E_{\downarrow\Rightarrow\downarrow} + \Delta E_{\uparrow\Rightarrow\uparrow} - \Delta E_{\uparrow\Rightarrow\downarrow} - \Delta E_{\downarrow\Rightarrow\uparrow}\,, \tag{5.2}$$

where each $\Delta E_{\sigma\Rightarrow\sigma'}$ is calculated by integrating over all the filled states with spin $\sigma \in \{\uparrow,\downarrow\}$ and all empty states with spin $\sigma' \in \{\uparrow,\downarrow\}$ as [144]

$$\Delta E_{\sigma\Rightarrow\sigma'} = \frac{\xi^2}{4} \sum_{\mu\mu'} P_{\mu\mu'} \int_{-\infty}^{E_F} \mathrm{d}\varepsilon \int_{E_F}^{\infty} \mathrm{d}\varepsilon' \frac{\varrho_{\mu}^{\sigma}(\varepsilon)\varrho_{\mu'}^{\sigma'}(\varepsilon')}{\varepsilon' - \varepsilon}\,. \tag{5.3}$$

Depending on the orbital character μ and μ' of the filled and empty states, respectively, the given virtual excitation has a contribution to E_{MCA} with a prefactor $P_{\mu\mu'}$, given in Tab. 5.1. Hence, in Eq. (5.3), there is a double summation over all filled and unfilled orbitals μ and μ', respectively, some of which contribute by a nonzero value according to $P_{\mu\mu'}$. The integrand is also proportional to the local orbital-resolved density of occupied and unoccupied states $\varrho_{\mu}^{\sigma}(\varepsilon)$ and $\varrho_{\mu'}^{\sigma'}(\varepsilon')$, respectively. From the denominator $\varepsilon' - \varepsilon$, it follows that the strongest contribution must come from the states around the Fermi level, where the occupied energy levels ε and unoccupied energy levels ε' are close to each other.

We apply Eq. (5.2)-Eq. (5.3) to the DOS of bulk bcc Co, in an attempt to reproduce the results of Fig. 3.6 [3]. In Fig. 5.2, we show the resulting four terms of Eq. (5.2), their

[3]Note that a DOS calculated from the self-consistent calculation [step 2 in Sec. 3.1] is used. Thereby, we do not need to perform the most expensive steps 3 and 4 (the calculations with SOC).

Table 5.1: Components of the $P_{\mu\mu'}$ matrix from Eq. (5.3) for d orbitals. (The virtual excitations involving s and p electrons are almost irrelevant, as only the d-orbitals are responsible for magnetism in $3d$-elements.) The matrix is defined as $P_{\mu\mu'} = |\langle\mu|L_z|\mu'\rangle|^2 - |\langle\mu|L_x|\mu'\rangle|^2$, where L_z and L_x are the orbital momentum operators in the z and x direction, respectively.

$P_{\mu\mu'}$	d_{xy}	d_{yz}	d_{z^2}	d_{xz}	d_{x^2}
d_{xy}	0	0	0	-1	4
d_{yz}	0	0	-3	1	-1
d_{z^2}	0	-3	0	0	0
d_{xz}	-1	1	0	0	0
d_{x^2}	4	-1	0	0	0

sum ("E_{MCA}"), and the curve for bcc Co from Fig. 3.6 that we try to reproduce ("DFT"). The E_{MCA} curve does not reproduce the DFT curve well, so the model of Eq. (5.3) must be an oversimplification, and a more precise treatment based on the band structure will be needed. Despite that, from Fig. 5.2(a), we can already draw several qualitative conclusions.

1. The minority-to-minority excitation contribution $\Delta E_{\downarrow\Rightarrow\downarrow}$ (the only term taken into account in the original Bruno approach [141]) on its own can reproduce the increase of E_{MCA} for $c/a < 1$ observed in the DFT curve. Therefore, in Fig. 5.2(b), we analyze $\Delta E_{\downarrow\Rightarrow\downarrow}$ in more detail and show all its excitation contributions separately. We see that the increase is caused by excitations from d_{yz} to d_{z^2} minority orbitals and vice versa ($d_{yz} \leftrightarrow d_{z^2}$).

   This behavior is linked to the strain-induced changes in the LDOS: for $c/a < 1$ [Fig. 5.2(e)], the d_{z^2} peak in the empty minority states is shifted further above the Fermi level. Because of the $\varepsilon' - \varepsilon$ denominator in Eq. (5.3), this weakens all the contributions involving d_{z^2} minority empty states, namely the negative $d_{yz} \rightarrow d_{z^2}$ contribution (the contribution with the largest negative prefactor of -3, see Tab. 5.1). The weakening of this negative contribution then increases the overall E_{MCA}.

   The increase is counteracted by a decrease in the positive $d_{xy} \leftrightarrow d_{x^2-y^2}$ excitation. This decrease is due to the strain-induced shift of the minority empty $d_{x^2-y^2}$ peak, located immediately above E_F for $c/a = 1$.

2. The two contributions that come from excitations to majority-spin states, $\Delta E_{\uparrow\Rightarrow\uparrow}$ and $-\Delta E_{\downarrow\Rightarrow\uparrow}$, are small. The reason is that there are almost no empty majority-spin states, especially near the Fermi level, as we see in Fig. 5.2(d)-Fig. 5.2(f). Moreover, $\Delta E_{\uparrow\Rightarrow\uparrow}$ and $-\Delta E_{\downarrow\Rightarrow\uparrow}$ tend to cancel each other. Hence they can often be neglected [144].

Note that including the p-orbital excitations gives only a minor correction of approximately 1%.

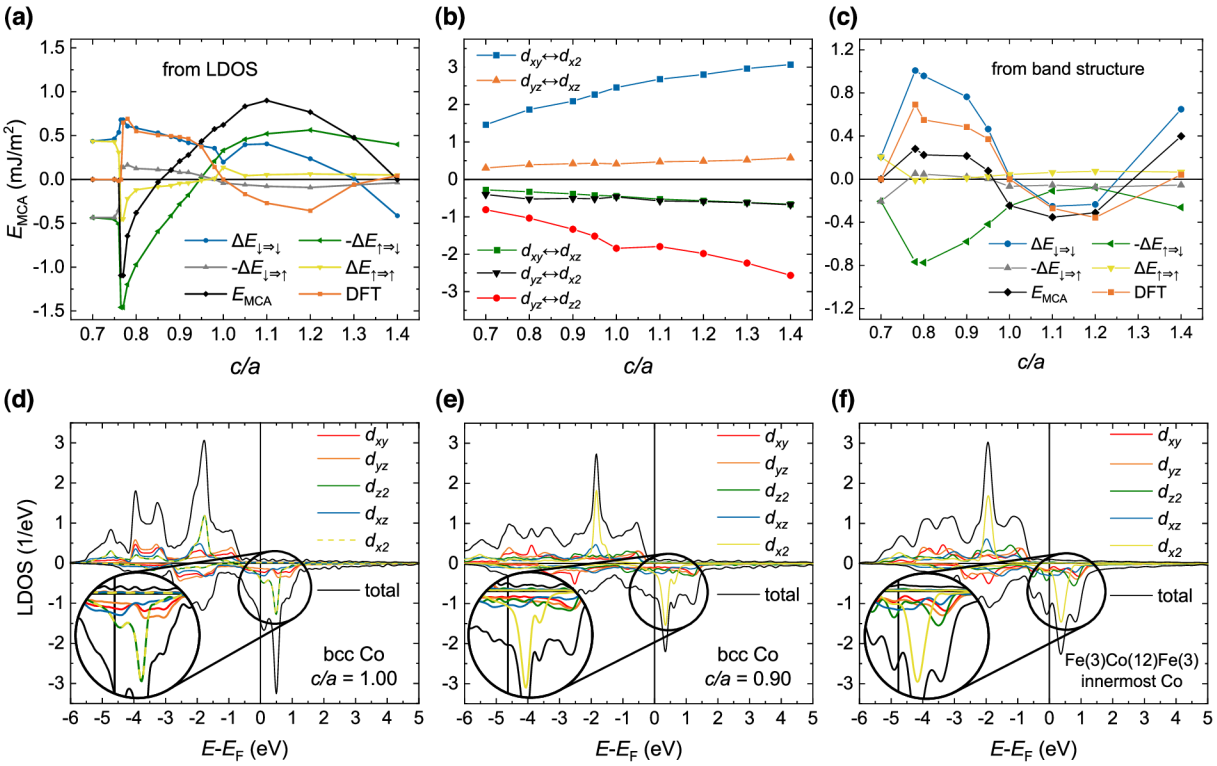

Figure 5.2: (a) Based on the orbital-resolved local density of states, the four contributions to the bcc Co $E_{\mathrm{MCA}}(c/a)$ calculated from the second-order perturbation theory [143] are shown separately and in total. The values extracted from the DFT calculation with spin-orbit coupling included ["DFT"; see Fig. 3.6] are shown for comparison. The classical Bruno term $\Delta E_{\downarrow\Rightarrow\downarrow}$ on its own reproduces the DFT curve for $c/a < 1$ to a certain extent. (b) The Bruno $\Delta E_{\downarrow\Rightarrow\downarrow}$ term from (a) divided into contributions from individual virtual excitations. The excitation from d_{yz} to d_{z^2} states and vice versa ($d_{yz} \leftrightarrow d_{z^2}$; red circles) is the one that causes the overall increase for $c/a < 1$. (c) Same as (a) but calculated from the orbital-projected band structure, where additional aspects are taken into account (see text for details). The correspondence with the DFT curve is hence much better. (d) The orbital-resolved DOS for bcc Co with $c/a = 1$. There is a peak in the d_{z^2} and $d_{x^2-y^2}$ minority states right above the Fermi level. (e) The orbital-resolved DOS for bcc Co with $c/a = 0.90$. The strain causes the overall spreading of the DOS. Both the d_{z^2} and the $d_{x^2-y^2}$ peaks are pushed further above E_F. (f) The most bulklike Co from the Fe(3)Co(12)Fe(3) structure. Its features are very similar to the bcc Co with $c/a = 0.90$ in (e), supporting the applicability of the results of the PT2 approach to the proposed structures of Chapter 4. © 2021 American Physical Society [120].

5.3. Band structure-based E_{MCA} calculation

To redeem the inaccuracy of the DOS-based model, the next step is to calculate E_{MCA} directly from the (orbital-resolved) band structure. This approach takes into account many aspects that were neglected in the calculation from LDOS. The equations are given in Ref. [143, Eqs. (4)–(6)]. The orbital-resolved PROCAR file (Sec. 2.13) is needed as an input. One also needs to set `LORBIT=12` in the INCAR, to obtain both the real and imaginary parts of the projection coefficients c in PROCAR. The c coefficients are used to calculate the joint local density of states G [Eq. 4 in Ref. [143])]. Taking the real part of G and performing summation over several variables, one finally obtains the four contributions to E_{MCA} from Eq. (5.2).

The difference compared to the DOS-based approach boils down to three important points:

1. the projection coefficient of a Bloch state onto a particular d orbital is considered properly as a complex number, not just as its magnitude;

2. virtual excitations also happen in between atoms at different sites, not only on-site; and

3. the mechanism of a virtual excitation generally includes four orbitals, not only two (see Fig. 1 in Ref. [145]).

All these three features have proven to be essential for the model to be more accurate.

The band structure calculation results are plotted in Fig. 5.2(c). We use $\xi_{\mathrm{Co}} = 84$ meV [142]. The model is much better than the one in Fig. 5.2(a), while the main features are retained, namely that the $\Delta E_{\downarrow\Rightarrow\downarrow}$ term governs the overall trend.

The $-\Delta E_{\uparrow\Rightarrow\downarrow}$ term serves to refine the shape, but in addition, causes an excessive overall decrease. The $E_{\mathrm{MCA}}(c/a = 1)$ is not zero in the E_{MCA} curve, as it should be by symmetry arguments and as it is in the DFT curve. Despite that, the difference $E_{\mathrm{MCA}}(c/a = 0.90) - E_{\mathrm{MCA}}(c/a = 1.00)$ in the E_{MCA} curve and DFT curves correspond well to each other. Analyzing the contributions to $\Delta E_{\downarrow\Rightarrow\downarrow}$ from individual excitations, we confirm the results of Sec. 5.2, namely that the main positive change in E_{MCA} for $c/a < 1$ is due to the $d_{yz} \rightarrow d_{z^2}$ virtual excitation, and the main negative change is due to the $d_{x^2-y^2} \rightarrow d_{xy}$ excitation.

Conclusion

To conclude, we introduced the importance of MgO-based magnetic tunnel junctions (MTJ) both for the traditional hard drives and the emerging spin-transfer torque magnetic random-access memory (STT-MRAM). STT-MRAM has already entered volume production and has a strong potential for applications, notably to replace SRAM and DRAM in certain memory hierarchy levels to make electronic devices more power-efficient (Fig. 3).

The different types of magnetic anisotropy were given, along with their fundamental physical origins. We showed how the magnetic anisotropy is crucial for magnetic memory stability, especially when downscaling the memory bits.

We then developed the fundamentals of density functional theory, the main method used in this work to perform ab initio calculations. The basic inputs and outputs of the Vienna ab initio simulation package (VASP) were outlined.

Next, we proceeded to our results of the systematic study of perpendicular magnetic anisotropy (PMA) in MgO-based MTJs with bcc Fe, Co, and Ni as a storage layer (Fig. 3.5). We do observe the well-known interfacial PMA of Fe/MgO (Fig. 3.4) and confirm its origin, which is the hybridization between the interfacial Fe and O (Fig. 3.3). Interestingly, we found a large bulk PMA within bcc Co/MgO and explain it in terms of the MgO-induced strain. We confirmed the effect quantitatively by calculating the PMA in a simple strained bcc Co unit cell (Fig. 3.6).

We exploited these findings and proposed an MTJ with a simple design and strongly enhanced PMA in the form Fe/Co/Fe|MgO (Fig. 4.1). Replacing the bulk-like Fe layers with bcc Co indeed provides a large strain-induced contribution [Fig. 4.2(a)]. We implemented an atomistic calculation of the demagnetizing energy (Fig. 4.3) and showed that there is a second benefit of the Fe/Co/Fe|MgO design, which comes from reducing the negative demagnetizing energy. The overall result is a strongly enhanced PMA, increasing with the Co thickness (Fig. 4.4). We discussed the decrease of PMA upon Fe/Co interdiffusion, the limitations of fabricating metastable bcc Co, and estimated the tunneling magnetoresistance of the MTJs, which is large.

Finally, encouraged by the good applicability of Bruno's model to the studied systems (Fig. 5.1), we implemented a code based on the second-order perturbation theory to calculate PMA directly from the density of states or band structure. This gave us further insight into the behavior of PMA in response to the changes in the electronic structure. Namely, we reproduced well the c/a dependence of PMA in strained bcc Co (Fig. 5.2) and attributed its large strain-induced value to the changes in the d_{yz} and d_{z^2} minority states.

References

[1] DIENY, B. and M. CHSHIEV. Perpendicular Magnetic Anisotropy at Transition Metal/Oxide Interfaces and Applications. *Reviews of Modern Physics*. 2017, **89**(2), p. 025008. ISSN 0034-6861, 1539-0756. Available from: doi:10.1103/RevModPhys.89.025008.

[2] ZHU, Jian-Gang (Jimmy) and Chando PARK. Magnetic Tunnel Junctions. *Materials Today*. 2006, **9**(11), p. 36–45. ISSN 13697021. Available from: doi:10.1016/S1369-7021(06)71693-5.

[3] JULLIERE, M. Tunneling between Ferromagnetic Films. *Physics Letters A*. 1975, **54**(3), p. 225–226. ISSN 03759601. Available from: doi:10.1016/0375-9601(75)90174-7.

[4] MOODERA, J. S. et al. Large Magnetoresistance at Room Temperature in Ferromagnetic Thin Film Tunnel Junctions. *Physical Review Letters*. 1995, **74**(16), p. 3273–3276. ISSN 0031-9007, 1079-7114. Available from: doi:10.1103/PhysRevLett.74.3273.

[5] HAN, XiuFeng, Syed Shahbaz ALI and ShiHeng LIANG. MgO(001) Barrier Based Magnetic Tunnel Junctions and Their Device Applications. *Science China Physics, Mechanics and Astronomy*. 2013, **56**(1), p. 29–60. ISSN 1674-7348, 1869-1927. Available from: doi:10.1007/s11433-012-4977-1.

[6] HIROHATA, Atsufumi et al. Review on Spintronics: Principles and Device Applications. *Journal of Magnetism and Magnetic Materials*. 2020, **509**, p. 166711. ISSN 03048853. Available from: doi:10.1016/j.jmmm.2020.166711.

[7] BAJOREK, Christopher H. Magnetoresistive (MR) Heads and the Earliest MR Head-Based Disk Drives: Sawmill and Corsair, Computer History Museum, Mountain View, CA, Tech. Rep. 2014,

[8] BHATTI, Sabpreet et al. Spintronics Based Random Access Memory: A Review. *Materials Today*. 2017, **20**(9), p. 530–548. ISSN 13697021. Available from: doi:10.1016/j.mattod.2017.07.007.

[9] STEPHAN, Andrew W. and Steven J. KOESTER. Spin Hall MTJ Devices for Advanced Neuromorphic Functions. *IEEE Transactions on Electron Devices*. 2020, **67**(2), p. 487–492. ISSN 0018-9383, 1557-9646. Available from: doi:10.1109/TED.2019.2959732.

[10] CHOI, Won Ho et al. A Magnetic Tunnel Junction Based True Random Number Generator with Conditional Perturb and Real-Time Output Probability Tracking. In: *2014 IEEE International Electron Devices Meeting*. 2014, p. 12–5.

[11] MAEHARA, Hiroki et al. High Q Factor over 3000 Due to Out-of-Plane Precession in Nano-Contact Spin-Torque Oscillator Based on Magnetic Tunnel Junctions. *Applied Physics Express*. 2014, **7**(2), p. 023003. ISSN 1882-0778, 1882-0786. Available from: doi:10.7567/APEX.7.023003.

[12] BORDERS, William A et al. Integer Factorization Using Stochastic Magnetic Tunnel Junctions. *Nature*. 2019, **573**(7774), p. 390–393.

[13] SCHALLER, R.R. Moore's Law: Past, Present and Future. *IEEE Spectrum*. 1997, **34**(6), p. 52–59. ISSN 0018-9235. Available from: doi:10.1109/6.591665.

[14] REINSEL, David, John GANTZ and John RYDNING. The Digitization of the World from Edge to Core. *Framingham: International Data Corporation*. 2018, p. 28.

[15] BUTLER, W. H. et al. Spin-Dependent Tunneling Conductance of Fe | MgO | Fe Sandwiches. *Physical Review B*. 2001, **63**(5), p. 054416. ISSN 0163-1829, 1095-3795. Available from: doi:10.1103/PhysRevB.63.054416.

[16] BUTLER, W.H. et al. Theory of tunneling magnetoresistance for epitaxial systems. *IEEE Transactions on Magnetics* [online]. 2005, [visited on 2021-05-19], **41**(10), p. 2645–2648. ISSN 0018-9464. Available from: doi:10.1109/TMAG.2005.854763. Available from: http://ieeexplore.ieee.org/document/1519075/.

[17] MATHON, J. and A. UMERSKI. Theory of Tunneling Magnetoresistance of an Epitaxial Fe/MgO/Fe(001) Junction. *Physical Review B*. 2001, **63**(22), p. 220403. ISSN 0163-1829, 1095-3795. Available from: doi:10.1103/PhysRevB.63.220403.

[18] FREEDMAN, Alan and Irma MORRISON. *ComputerLanguage.com: Perpendicular Recording - CLC Definition* [online]. Available from: https://www.computerlanguage.com/. Accessed: 2021-05-14.

[19] RE, Mark. *Internet Archive: Tech Talk on HDD Areal Density* [online]. Available from: https://web.archive.org/. Accessed: 2021-05-14.

[20] YOON, Alex. *Lam Research: Tech Brief: ABCs of New Memory* [online]. Available from: https://blog.lamresearch.com/. Accessed: 2021-05-14.

[21] ZHAO, Weisheng and Guillaume PRENAT. *Spintronics-Based Computing*. Cham: Springer International Publishing, 2015. ISBN 978-3-319-15179-3 978-3-319-15180-9. Available from: doi:10.1007/978-3-319-15180-9.

[22] WONG, Bill. The Fundamentals Of Flash Memory Storage. *Electronic Design* [online]. 2012, **60**(4), p. 34. Available from: https://www.electronicdesign.com/technologies/memory/.

[23] SINGH, Jawar, Saraju P MOHANTY and Dhiraj K PRADHAN. *Robust SRAM designs and analysis*. Springer Science & Business Media, 2012.

[24] EVERSPIN TECHNOLOGIES, Inc. *Everspin Begins 40nm STT-MRAM Volume Production | Everspin Technologies Inc.* [online]. Available from: https://investor.everspin.com/. Accessed: 2021-05-14.

[25] SLONCZEWSKI, J.C. Current-Driven Excitation of Magnetic Multilayers. *Journal of Magnetism and Magnetic Materials*. 1996, **159**(1-2), p. L1–L7. ISSN 03048853. Available from: doi:10.1016/0304-8853(96)00062-5.

[26] BERGER, L. Emission of Spin Waves by a Magnetic Multilayer Traversed by a Current. *Physical Review B*. 1996, **54**(13), p. 9353–9358. ISSN 0163-1829, 1095-3795. Available from: doi:10.1103/PhysRevB.54.9353.

[27] KENT, Andrew D. Perpendicular All the Way. *Nature Materials*. 2010, **9**(9), p. 699–700. ISSN 1476-1122, 1476-4660. Available from: doi:10.1038/nmat2844.

[28] IKEDA, S. et al. A Perpendicular-Anisotropy CoFeB–MgO Magnetic Tunnel Junction. *Nature Materials*. 2010, **9**(9), p. 721–724. ISSN 1476-1122, 1476-4660. Available from: doi:10.1038/nmat2804.

[29] BLUNDELL, S. *Magnetism in Condensed Matter*. Oxford ; New York: Oxford University Press, 2001. Oxford Master Series in Condensed Matter Physics. ISBN 978-0-19-850592-1.

[30] COEY, J.M.D. *Magnetism and Magnetic Materials*. Cambridge: Cambridge University Press, 2010. ISBN 978-0-511-67743-4.

[31] MOHN, Peter. *Magnetism in the Solid State: An Introduction*. Corrected 2nd printing. Berlin ; New York: Springer, 2006. Springer Series in Solid-State Sciences. ISBN 978-3-540-29384-2.

[32] BRUNO, Patrick. Physical Origins and Theoretical Models of Magnetic Anisotropy. In: *Ferienkurse Des Forschungszentrums Julich*. 1993, p. 29.

[33] GRIFFITHS, David J. and Darrell F. SCHROETER. *Introduction to Quantum Mechanics*. Third. Cambridge University Press, 2018. ISBN 978-1-316-99543-3 978-1-107-18963-8. Available from: doi:10.1017/9781316995433.

[34] JONES, William and Norman Henry MARCH. *Theoretical Solid State Physics*. Courier Corporation, 1985.

[35] IBRAHIM, Fatima. *Theoretical Study of Electronic Structure and Magnetism in Materials for Spintronics*. 2014. PhD thesis. Strasbourg.

[36] ARGYRES, P.N. Theory of the Faraday and Kerr Effects in Ferromagnetics. *Physical Review*. 1955, **97**(2), p. 334–345. ISSN 0031-899X. Available from: doi:10.1103/PhysRev.97.334.

[37] MARTIN, Richard M. *Electronic Structure: Basic Theory and Practical Methods*. Second. Cambridge University Press, 2020. ISBN 978-1-108-55558-6 978-1-108-42990-0. Available from: doi:10.1017/9781108555586.

[38] CHRISTENSEN, N Egede and BO SERAPHIN. Relativistic Band Calculation and the Optical Properties of Gold. *Physical Review B*. 1971, **4**(10), p. 3321.

[39] KITTEL, Charles. *Introduction to Solid State Physics*. 8th ed. Hoboken, NJ: Wiley, 2005. ISBN 978-0-471-41526-8.

[40] DIRAC, P. A. M. Quantum Mechanics of Many-Electron Systems. *Proceedings of the Royal Society of London. Series A, Containing Papers of a Mathematical and Physical Character*. 1929, **123**(792), p. 714–733.

[41] *The Nobel Prize in Chemistry 1998*. [online]. [Visited on 2021-05-19]. Available from: https://www.nobelprize.org/prizes/chemistry/1998/summary/.

[42] HAUNSCHILD, Robin, Andreas BARTH and Werner MARX. Evolution of DFT Studies in View of a Scientometric Perspective. *Journal of Cheminformatics*. 2016, **8**(1), p. 52. ISSN 1758-2946. Available from: doi:10.1186/s13321-016-0166-y.

[43] CAPELLE, Klaus. A Bird's-Eye View of Density-Functional Theory. *arXiv:cond-mat/0211443* [online]. 2006, Comment: v5: 69 pages, 3 figures. Major revision and extension of previous versions, reflecting publication of this paper, which was so far only available electronically (and in a very preliminary version as a book chapter), as a review paper in the Brazilian Journal of Physics.

[44] BURKE, Kieron and Lucas O. WAGNER. DFT in a Nutshell. *International Journal of Quantum Chemistry*. 2013, **113**(2), p. 96–101. ISSN 00207608. Available from: doi:10.1002/qua.24259.

[45] HARRISON, NM. An introduction to density functional theory. *Nato Science Series Sub Series III Computer and Systems Sciences*. 2003, **187**, p. 45–70.

[46] BIHLMAYER, Gustav. Density Functional Theory for Magnetism and Magnetic Anisotropy. In: *Handbook of Materials Modeling*. Cham: Springer International Publishing, 2018, p. 1–23. ISBN 978-3-319-42913-7. Available from: doi:10.1007/978-3-319-42913-7_73-1.

[47] CHOY, Tat Sang. *The Fermi Surface Database* [online]. Available from: http://www.phys.ufl.edu/fermisurface/. Accessed: 2021-05-14.

[48] MATERIALSPROJECT. *Bcc Fe*. LBNL Materials Project; Lawrence Berkeley National Laboratory (LBNL), Berkeley, CA (United States), 2020. Available from: doi:10.17188/1189317.

[49] BECHSTEDT, Friedhelm. *Many-Body Approach to Electronic Excitations*. Berlin, Heidelberg: Springer Berlin Heidelberg, 2015. Springer Series in Solid-State Sciences. ISBN 978-3-662-44592-1 978-3-662-44593-8. Available from: doi:10.1007/978-3-662-44593-8.

[50] HARTREE, Douglas Rayne. The Wave Mechanics of an Atom with a Non-Coulomb Central Field. Part II. Some Results and Discussion. In: *Mathematical Proceedings of the Cambridge Philosophical Society*. 1928, p. 111–132.

[51] BORN, M. and R. OPPENHEIMER. Zur Quantentheorie der Molekeln. *Annalen der Physik*. 1927, **389**(20), p. 457–484. ISSN 00033804, 15213889. Available from: doi:10.1002/andp.19273892002.

[52] JENKINS, Stephen. *The Many Body Problem and Density Functional Theory* [online]. 1997. Available from: http://newton.ex.ac.uk/. Accessed: 2021-05-14.

[53] FOCK, Vladimir. Näherungsmethode Zur Lösung Des Quantenmechanischen Mehrkörperproblems. *Zeitschrift für Physik*. 1930, **61**(1-2), p. 126–148.

[54] SLATER, J. C. The Self Consistent Field and the Structure of Atoms. *Physical Review*. 1928, **32**(3), p. 339–348. ISSN 0031-899X. Available from: doi:10.1103/PhysRev.32.339.

[55] SUTTON, Adrian P. *Electronic Structure of Materials*. Oxford : New York: Clarendon Press ; Oxford University Press, 1993. Oxford Science Publications. ISBN 978-0-19-851755-9 978-0-19-851754-2.

[56] CRAMER, Christopher J. *Essentials of Computational Chemistry: Theories and Models*. John Wiley & Sons, 2013.

[57] GRIFFITHS, D.J. *Introduction to Electrodynamics*. Cambridge University Press, 2017. ISBN 978-1-108-35714-2.

[58] LEVY, Mel and John P PERDEW. Hellmann-Feynman, Virial, and Scaling Requisites for the Exact Universal Density Functionals. Shape of the Correlation Potential and Diamagnetic Susceptibility for Atoms. *Physical Review A*. 1985, **32**(4), p. 2010.

[59] THOMAS, L. H. The Calculation of Atomic Fields. *Mathematical Proceedings of the Cambridge Philosophical Society*. 1927, **23**(5), p. 542–548. ISSN 0305-0041, 1469-8064. Available from: doi:10.1017/S0305004100011683.

[60] FERMI, Enrico. Un Metodo Statistico per La Determinazione Di Alcune Priorieta Dell'atome. *Rend. Accad. Naz. Lincei*. 1927, **6**(602-607), p. 32.

[61] DIRAC, P. A. M. Note on Exchange Phenomena in the Thomas Atom. *Mathematical Proceedings of the Cambridge Philosophical Society*. 1930, **26**(3), p. 376–385. ISSN 0305-0041, 1469-8064. Available from: doi:10.1017/S0305004100016108.

[62] V WEIZSÄCKER, CF. Zur Theorie Der Kernmassen. *Zeitschrift für Physik*. 1935, **96**(7-8), p. 431–458.

[63] TELLER, Edward. On the Stability of Molecules in the Thomas-Fermi Theory. *Reviews of Modern Physics*. 1962, **34**(4), p. 627–631. ISSN 0034-6861. Available from: doi:10.1103/RevModPhys.34.627.

[64] HOHENBERG, P. and W. KOHN. Inhomogeneous Electron Gas. *Physical Review*. 1964, **136**(3B), p. B864–B871. ISSN 0031-899X. Available from: doi:10.1103/PhysRev.136.B864.

[65] LEVY, Mel. Universal Variational Functionals of Electron Densities, First-Order Density Matrices, and Natural Spin-Orbitals and Solution of the v-Representability Problem. *Proceedings of the National Academy of Sciences*. 1979, **76**(12), p. 6062–6065.

[66] LEVY, Mel. Electron Densities in Search of Hamiltonians. *Physical Review A*. 1982, **26**(3), p. 1200.

[67] LIEB, Elliott H. Density Functionals for Coulomb Systems. *International Journal of Quantum Chemistry*. 1983, **24**(3), p. 243–277. ISSN 0020-7608, 1097-461X. Available from: doi:10.1002/qua.560240302.

[68] Von BARTH, U and L HEDIN. A Local Exchange-Correlation Potential for the Spin Polarized Case. i. *Journal of Physics C: Solid State Physics*. 1972, **5**(13), p. 1629–1642. ISSN 0022-3719. Available from: doi:10.1088/0022-3719/5/13/012.

[69] VIGNALE, G and Mark RASOLT. Current-and Spin-Density-Functional Theory for Inhomogeneous Electronic Systems in Strong Magnetic Fields. *Physical Review B*. 1988, **37**(18), p. 10685.

[70] MERMIN, N. David. Thermal Properties of the Inhomogeneous Electron Gas. *Physical Review*. 1965, **137**(5A), p. A1441–A1443. ISSN 0031-899X. Available from: doi:10.1103/PhysRev.137.A1441.

[71] RUNGE, Erich and Eberhard KU GROSS. Density-Functional Theory for Time-Dependent Systems. *Physical Review Letters*. 1984, **52**(12), p. 997.

[72] MARTIN, Richard M and Gerardo ORTIZ. Functional Theory of Extended Coulomb Systems. *Physical Review B*. 1997, **56**(3), p. 1124.

[73] HARRISON, Walter A. *Electronic Structure and the Properties of Solids: The Physics of the Chemical Bond*. Courier Corporation, 2012.

[74] KOHN, W. and L. J. SHAM. Self-Consistent Equations Including Exchange and Correlation Effects. *Physical Review*. 1965, **140**(4A), p. A1133–A1138. ISSN 0031-899X. Available from: doi:10.1103/PhysRev.140.A1133.

[75] DEDERICHS, P. H. and R. ZELLER. Self-Consistency Iterations in Electronic-Structure Calculations. *Physical Review B*. 1983, **28**(10), p. 5462–5472. ISSN 0163-1829. Available from: doi:10.1103/PhysRevB.28.5462.

[76] PICKETT, Warren E. Pseudopotential methods in condensed matter applications. *Computer Physics Reports*. 1989, **9**(3), p. 115–197.

[77] BROYDEN, C. G. A Class of Methods for Solving Nonlinear Simultaneous Equations. *Mathematics of Computation*. 1965, **19**(92), p. 577–577. ISSN 0025-5718. Available from: doi:10.1090/S0025-5718-1965-0198670-6.

[78] GARZA, Alejandro J. and Gustavo E. SCUSERIA. Comparison of Self-Consistent Field Convergence Acceleration Techniques. *The Journal of Chemical Physics*. 2012, **137**(5), p. 054110. ISSN 0021-9606, 1089-7690. Available from: doi:10.1063/1.4740249.

[79] CEPERLEY, David M and Berni J ALDER. Ground State of the Electron Gas by a Stochastic Method. *Physical review letters*. 1980, **45**(7), p. 566.

[80] PERDEW, J. P. and Alex ZUNGER. Self-Interaction Correction to Density-Functional Approximations for Many-Electron Systems. *Physical Review B*. 1981, **23**(10), p. 5048–5079. ISSN 0163-1829. Available from: doi:10.1103/PhysRevB.23.5048.

[81] JONES, R O and O GUNNARSSON. The Density Functional Formalism, Its Applications and Prospects. *Rev. Mod. Phys.* 1989, **61**(3), p. 58.

[82] GUNNARSSON, O, M JONSON and BI LUNDQVIST. Descriptions of Exchange and Correlation Effects in Inhomogeneous Electron Systems. *Physical Review B*. 1979, **20**(8), p. 3136.

[83] GROSS, Hardy. *L03, Hardy Gross, Exchange-Correlation Functionals* [online]. 2017. Available from: https://www.youtube.com/watch?v=dhaI8xXY_fo&list=PLbgFiRV2JFy-VQ3D6cJjn5jkXmAsjQPiT&index=3&ab_channel=fhitheoryfhitheory. Accessed: 2021-05-14.

[84] BECKE, A. D. Density-Functional Exchange-Energy Approximation with Correct Asymptotic Behavior. *Physical Review A*. 1988, **38**(6), p. 3098–3100. ISSN 0556-2791. Available from: doi:10.1103/PhysRevA.38.3098.

[85] PERDEW, John P. and Yue WANG. Accurate and Simple Analytic Representation of the Electron-Gas Correlation Energy. *Physical Review B*. 1992, **45**(23), p. 13244–13249. ISSN 0163-1829, 1095-3795. Available from: doi:10.1103/PhysRevB.45.13244.

[86] PERDEW, John P, Kieron BURKE and Matthias ERNZERHOF. Generalized Gradient Approximation Made Simple. *PHYSICAL REVIEW LETTERS*. 1996, **77**(18), p. 4.

[87] PERDEW, John P., Kieron BURKE and Matthias ERNZERHOF. Generalized Gradient Approximation Made Simple. *Physical Review Letters*. 1996, **77**(18), p. 3865–3868. ISSN 0031-9007, 1079-7114. Available from: doi:10.1103/PhysRevLett.77.3865.

[88] MARDIROSSIAN, Narbe and Martin HEAD-GORDON. Thirty Years of Density Functional Theory in Computational Chemistry: An Overview and Extensive Assessment of 200 Density Functionals. *Molecular Physics*. 2017, **115**(19), p. 2315–2372.

[89] GONZE, Xavier. *L07, Xavier Gonze, Plane-Wave Pseudopotentials and Projector Augmented Wave Methods*. 2017.

[90] BECK, Thomas L. Real-Space Mesh Techniques in Density-Functional Theory. *Reviews of Modern Physics*. 2000, **72**(4), p. 1041–1080. ISSN 0034-6861, 1539-0756. Available from: doi:10.1103/RevModPhys.72.1041.

[91] BLÖCHL, P. E. Projector Augmented-Wave Method. *Physical Review B*. 1994, **50**(24), p. 17953–17979. ISSN 0163-1829, 1095-3795. Available from: doi:10.1103/PhysRevB.50.17953.

[92] SLATER, J. C. and G. F. KOSTER. Simplified LCAO Method for the Periodic Potential Problem. *Physical Review*. 1954, **94**(6), p. 1498–1524. ISSN 0031-899X. Available from: doi:10.1103/PhysRev.94.1498.

[93] SINGH, David J and Lars NORDSTROM. *Planewaves, Pseudopotentials, and the LAPW Method*. Springer Science & Business Media, 2006. ISBN 978-1-4614-0817-8.

[94] SLATER, J. C. Wave Functions in a Periodic Potential. *Physical Review*. 1937, **51**(10), p. 846–851. ISSN 0031-899X. Available from: doi:10.1103/PhysRev.51.846.

[95] KORRINGA, J. On the Calculation of the Energy of a Bloch Wave in a Metal. *Physica*. 1947, **13**(6-7), p. 392–400.

[96] KOHN, Wo and No ROSTOKER. Solution of the Schrödinger Equation in Periodic Lattices with an Application to Metallic Lithium. *Physical Review*. 1954, **94**(5), p. 1111.

[97] ANDERSEN, Ole Krogh and Ove JEPSEN. Explicit, First-Principles Tight-Binding Theory. *Physical Review Letters*. 1984, **53**(27), p. 2571.

[98] SCUSERIA, Gustavo E. Linear Scaling Density Functional Calculations with Gaussian Orbitals. *The Journal of Physical Chemistry A*. 1999, **103**(25), p. 4782–4790.

[99] KIEJNA, Adam et al. Comparison of the Full-Potential and Frozen-Core Approximation Approaches to Density-Functional Calculations of Surfaces. *Physical Review B*. 2006, **73**(3), p. 035404. ISSN 1098-0121, 1550-235X. Available from: doi:10.1103/PhysRevB.73.035404.

[100] KAXIRAS, Efthimios. *Atomic and Electronic Structure of Solids*. First. Cambridge University Press, 2003. ISBN 978-0-521-81010-4 978-0-521-52339-4 978-0-511-75554-5. Available from: doi:10.1017/CBO9780511755545.

[101] QUESTER, Wolfram. *English: Comparison of a Wavefunction in the Coulomb Potential of the Nucleus (Blue) to the One in the Pseudopotential (Red). The Real and the Pseudo Wavefunction and Potentials Match above a Certain Cutoff Radius*. 22 November 2006 (original upload date).

[102] KRESSE, Georg. *Pseudopotentials (Part I):* [online]. Available from: https://cms.mpi.univie.ac.at/vasp-workshop/. Accessed: 2021-05-14.

[103] BIHLMAYER, Gustav. Density Functional Theory for Magnetism and Magnetic Anisotropy. In: *Handbook of Materials Modeling*. Cham: Springer International Publishing, 2018, p. 1–23. ISBN 978-3-319-42913-7. Available from: doi:10.1007/978-3-319-42913-7_73-1.

[104] TRYGG, J. et al. Total Energy Calculation of the Magnetocrystalline Anisotropy Energy in the Ferromagnetic 3 d Metals. *Physical Review Letters*. 1995, **75**(15), p. 2871–2874. ISSN 0031-9007, 1079-7114. Available from: doi:10.1103/PhysRevLett.75.2871.

[105] WANG, Xindong et al. Validity of the Force Theorem for Magnetocrystalline Anisotropy. *Journal of Magnetism and Magnetic Materials*. 1996, **159**(3), p. 337–341. ISSN 03048853. Available from: doi:10.1016/0304-8853(95)00936-1.

[106] WEINERT, M., R. E. WATSON and J. W. DAVENPORT. Total-Energy Differences and Eigenvalue Sums. *Physical Review B*. 1985, **32**(4), p. 2115–2119. ISSN 0163-1829. Available from: doi:10.1103/PhysRevB.32.2115.

[107] WANG, Xindong et al. Torque method for the theoretical determination of magnetocrystalline anisotropy. *Physical Review B*. 1996, **54**(1), p. 61.

[108] KRESSE, Georg, Doris VOGTENHUBER and Martijn MARSMAN. *The VASP Manual* [online]. Available from: https://www.vasp.at/wiki/. Accessed: 2021-05-14.

[109] KRESSE, G. and J. HAFNER. *Ab Initio* Molecular Dynamics for Liquid Metals. *Physical Review B*. 1993, **47**(1), p. 558–561. ISSN 0163-1829, 1095-3795. Available from: doi:10.1103/PhysRevB.47.558.

[110] KRESSE, G. and J. FURTHMÜLLER. Efficiency of Ab-Initio Total Energy Calculations for Metals and Semiconductors Using a Plane-Wave Basis Set. *Computational Materials Science*. 1996, **6**(1), p. 15–50. ISSN 09270256. Available from: doi:10.1016/0927-0256(96)00008-0.

[111] Message passing interface (MPI). In: *Encyclopedia of parallel computing*: [online]. Boston, MA: Springer US, 2011, p. 1116–1116. ISBN 978-0-387-09766-4. Available from: doi:10.1007/978-0-387-09766-4 085. Available from: https://doi.org/10.1007/978-0-387-09766-4 085.

[112] GABRIEL, Edgar et al. Open MPI: Goals, Concept, and Design of a Next Generation MPI Implementation. In: *Proceedings, 11th European PVM/MPI Users' Group Meeting*. Budapest, Hungary: 2004, p. 97–104.

[113] WANG, Yue and John P. PERDEW. Correlation Hole of the Spin-Polarized Electron Gas, with Exact Small-Wave-Vector and High-Density Scaling. *Physical Review B*. 1991, **44**(24), p. 13298–13307. ISSN 0163-1829, 1095-3795. Available from: doi:10.1103/PhysRevB.44.13298.

[114] YANG, H. X. et al. First-Principles Investigation of the Very Large Perpendicular Magnetic Anisotropy at Fe | MgO and Co | MgO Interfaces. *Physical Review B*. 2011, **84**(5), p. 054401. ISSN 1098-0121, 1550-235X. Available from: doi:10.1103/PhysRevB.84.054401.

[115] HALLAL, A., B. DIENY and M. CHSHIEV. Impurity-Induced Enhancement of Perpendicular Magnetic Anisotropy in Fe/MgO Tunnel Junctions. *Physical Review B*. 2014, **90**(6), p. 064422. ISSN 1098-0121, 1550-235X. Available from: doi:10.1103/PhysRevB.90.064422.

[116] HELLMANN, Hans. *Hans Hellmann: Einführung in Die Quantenchemie: Mit Biografischen Notizen von Hans Hellmann Jr.* Springer-Verlag, 2015.

[117] FEYNMAN, Richard Phillips. Forces in Molecules. *Physical review*. 1939, **56**(4), p. 340.

[118] EICHLER, Andreas. *Sampling the Brillouin-Zone* [online]. Available from: https://www.vasp.at/. Accessed: 2021-05-14.

[119] HALLAL, A. et al. Anatomy of Perpendicular Magnetic Anisotropy in Fe/MgO Magnetic Tunnel Junctions: First-Principles Insight. *Physical Review B*. 2013, **88**(18), p. 184423. ISSN 1098-0121, 1550-235X. Available from: doi:10.1103/PhysRevB.88.184423.

[120] VOJÁČEK, Libor et al. Giant Perpendicular Magnetic Anisotropy Enhancement in MgO -Based Magnetic Tunnel Junction by Using Co / Fe Composite Layer. *Physical Review Applied*. 2021, **15**(2), p. 024017. ISSN 2331-7019. Available from: doi:10.1103/PhysRevApplied.15.024017.

[121] SMITH, Deane K and HR LEIDER. Low-Temperature Thermal Expansion of LiH, MgO and CaO. *Journal of Applied Crystallography*. 1968, **1**(4), p. 246–249.

[122] BASINSKI, Zbigniew Stanislaw, William HUME-ROTHERY and AL SUTTON. The Lattice Expansion of Iron. *Proceedings of the Royal Society of London. Series A. Mathematical and Physical Sciences*. 1955, **229**(1179), p. 459–467.

[123] SWINNEN, B et al. Thermal Lattice Expansion and Out-of-Plane Relaxation of Bcc-Co in Fe/Co Multilayers Observed with Perturbed Angular Correlation Spectroscopy. *EPL (Europhysics Letters)*. 1997, **37**(9), p. 621.

[124] BELTRÁN, Juan Ignacio, Lluis BALCELLS and Carlos MARTÍNEZ-BOUBETA. Interfacial Geometry Dependence of the Iron Magnetic Moment: The Case of MgO/Fe/MgO. *Physical Review B*. 2012, **85**(6), p. 064417. ISSN 1098-0121, 1550-235X. Available from: doi:10.1103/PhysRevB.85.064417.

[125] LI, Chun and A. J. FREEMAN. Giant Monolayer Magnetization of Fe on MgO: A Nearly Ideal Two-Dimensional Magnetic System. *Physical Review B*. 1991, **43**(1), p. 780–787. ISSN 0163-1829, 1095-3795. Available from: doi:10.1103/PhysRevB.43.780.

[126] JAL, Emmanuelle et al. Interface Fe Magnetic Moment Enhancement in MgO/Fe/MgO Trilayers. *Applied Physics Letters*. 2015, **107**(9), p. 092404. ISSN 0003-6951, 1077-3118. Available from: doi:10.1063/1.4929990.

[127] BURKERT, Till et al. Giant Magnetic Anisotropy in Tetragonal FeCo Alloys. *Physical Review Letters*. 2004, **93**(2), p. 027203. ISSN 0031-9007, 1079-7114. Available from: doi:10.1103/PhysRevLett.93.027203.

[128] BURKERT, Till et al. Calculation of Uniaxial Magnetic Anisotropy Energy of Tetragonal and Trigonal Fe, Co, and Ni. *Physical Review B*. 2004, **69**(10), p. 104426. ISSN 1098-0121, 1550-235X. Available from: doi:10.1103/PhysRevB.69.104426.

[129] DRAAISMA, H. J. G. and W. J. M. DE JONGE. Surface and Volume Anisotropy from Dipole-dipole Interactions in Ultrathin Ferromagnetic Films. *Journal of Applied Physics*. 1988, **64**(7), p. 3610–3613. ISSN 0021-8979, 1089-7550. Available from: doi:10.1063/1.341397.

[130] DAALDEROP, G. H. O., P. J. KELLY and M. F. H. SCHUURMANS. First-Principles Calculation of the Magnetocrystalline Anisotropy Energy of Iron, Cobalt, and Nickel. *Physical Review B*. 1990, **41**(17), p. 11919–11937. ISSN 0163-1829, 1095-3795. Available from: doi:10.1103/PhysRevB.41.11919.

[131] MOMMA, Koichi and Fujio IZUMI. *VESTA 3* for Three-Dimensional Visualization of Crystal, Volumetric and Morphology Data. *Journal of Applied Crystallography*. 2011, **44**(6), p. 1272–1276. ISSN 0021-8898. Available from: doi:10.1107/S0021889811038970.

[132] YUASA, Shinji et al. Giant Tunneling Magnetoresistance up to 410% at Room Temperature in Fully Epitaxial Co/MgO/Co Magnetic Tunnel Junctions with Bcc Co(001) Electrodes. *Applied Physics Letters*. 2006, **89**(4), p. 042505. ISSN 0003-6951, 1077-3118. Available from: doi:10.1063/1.2236268.

[133] KHVALKOVSKIY, A V et al. Basic Principles of STT-MRAM Cell Operation in Memory Arrays. *Journal of Physics D: Applied Physics*. 2013, **46**(7), p. 074001. ISSN 0022-3727, 1361-6463. Available from: doi:10.1088/0022-3727/46/7/074001.

[134] APALKOV, Dmytro, Bernard DIENY and J. M. SLAUGHTER. Magnetoresistive Random Access Memory. *Proceedings of the IEEE*. 2016, **104**(10), p. 1796–1830. ISSN 0018-9219, 1558-2256. Available from: doi:10.1109/JPROC.2016.2590142.

[135] LI, Hong and B. P. TONNER. Direct Experimental Identification of the Structure of Ultrathin Films of Bcc Iron and Metastable Bcc and Fcc Cobalt. *Physical Review B*. 1989, **40**(15), p. 10241–10248. ISSN 0163-1829. Available from: doi:10.1103/PhysRevB.40.10241.

[136] SUBRAMANIAN, S. et al. Magnetic Anisotropies in Body-Centered-Cubic Cobalt Films. *Physical Review B*. 1995, **52**(14), p. 10194–10201. ISSN 0163-1829, 1095-3795. Available from: doi:10.1103/PhysRevB.52.10194.

[137] LIU, X. et al. Magnetic Anisotropies in Thick Body Centered Cubic Co. *Journal of Applied Physics*. 1996, **79**(8), p. 5387. ISSN 00218979. Available from: doi:10.1063/1.362312.

[138] HOUDY, Ph. et al. Magnetic and Structural Properties of Rf-sputtered Co/Fe and Co/Cr Multilayers. *Journal of Applied Physics*. 1991, **69**(8), p. 5667–5669. ISSN 0021-8979, 1089-7550. Available from: doi:10.1063/1.347930.

[139] SANDER, D. The Magnetic Anisotropy and Spin Reorientation of Nanostructures and Nanoscale Films. *Journal of Physics: Condensed Matter*. 2004, **16**(20), p. R603–R636. ISSN 0953-8984, 1361-648X. Available from: doi:10.1088/0953-8984/16/20/R01.

[140] FALEEV, Sergey V, Oleg N MRYASOV and Mark VAN SCHILFGAARDE. Effect of Correlations on Electronic Structure and Transport across (001) Fe/MgO/Fe Junctions. *Physical Review B*. 2012, **85**(17), p. 174433.

[141] BRUNO, Patrick. Tight-Binding Approach to the Orbital Magnetic Moment and Magnetocrystalline Anisotropy of Transition-Metal Monolayers. *Physical Review B*. 1989, **39**(1), p. 865–868. ISSN 0163-1829. Available from: doi:10.1103/PhysRevB.39.865.

[142] POPESCU, V. et al. Spin and Orbital Magnetic Moments of 3 d and 4 d Impurities in and on the (001) Surface of Bcc Fe. *Physical Review B*. 2001, **64**(18), p. 184407. ISSN 0163-1829, 1095-3795. Available from: doi:10.1103/PhysRevB.64.184407.

[143] MIURA, Yoshio et al. The Origin of Perpendicular Magneto-Crystalline Anisotropy in L1 $_0$ –FeNi under Tetragonal Distortion. *Journal of Physics: Condensed Matter*. 2013, **25**(10), p. 106005. ISSN 0953-8984, 1361-648X. Available from: doi:10.1088/0953-8984/25/10/106005.

[144] ZHANG, Jia et al. Model of Orbital Populations for Voltage-Controlled Magnetic Anisotropy in Transition-Metal Thin Films. *Physical Review B*. 2017, **96**(1), p. 014435. ISSN 2469-9950, 2469-9969. Available from: doi:10.1103/PhysRevB.96.014435.

[145] Van der LAAN, Gerrit. Microscopic Origin of Magnetocrystalline Anisotropy in Transition Metal Thin Films. *Journal of Physics: Condensed Matter*. 1998, **10**(14), p. 3239–3253. ISSN 0953-8984, 1361-648X. Available from: doi:10.1088/0953-8984/10/14/012.

List of abbreviations

bcc	body-centered cubic
CPU	central processing unit
DFT	density functional theory
DOS	density of states
DRAM	dynamic random-access memory
fcc	face-centered cubic
GGA	generalized gradient approximation
HDD	hard disk drive
HK	Hohenberg-Kohn
KS	Kohn-Sham
LDA	local density approximation
LDOS	local density of states
ML	monolayer
MRAM	magnetoresistive random-access memory
MTJ	magnetic tunnel junction
PAW	projector augmented wave
PBE	Perdew-Burke-Ernzerhof
PMA	perpendicular magnetic anisotropy
PT2	second order perturbation theory
SOC	spin-orbit coupling
SRAM	static random-access memory
SSD	solid-state drive
STT-MRAM	spin-transfer torque magnetic random-access memory
TMR	tunneling magnetoresistance effect
VASP	Vienna Ab initio Simulation Package

A. Supporting ab initio results

In Fig. A.1, we plot the layer-resolved contributions to E_{MCA} in bcc metal/MgO for a whole range of metal thicknesses (5 ML to 15 ML). (In Fig. 3.5(b), only the 15 ML case was shown.) It is clear that the interfacial contributions remain almost unchanged across different thicknesses for Fe and Co, but in case of Ni, they change substantially.

In Fig. A.2, we provide the layer-resolved c/a ratios for the metal/MgO structures with different thicknesses.

Fig. A.3 compares the strain-dependent E_{MCA} from Fig. 3.6 with the values from Ref. [127].

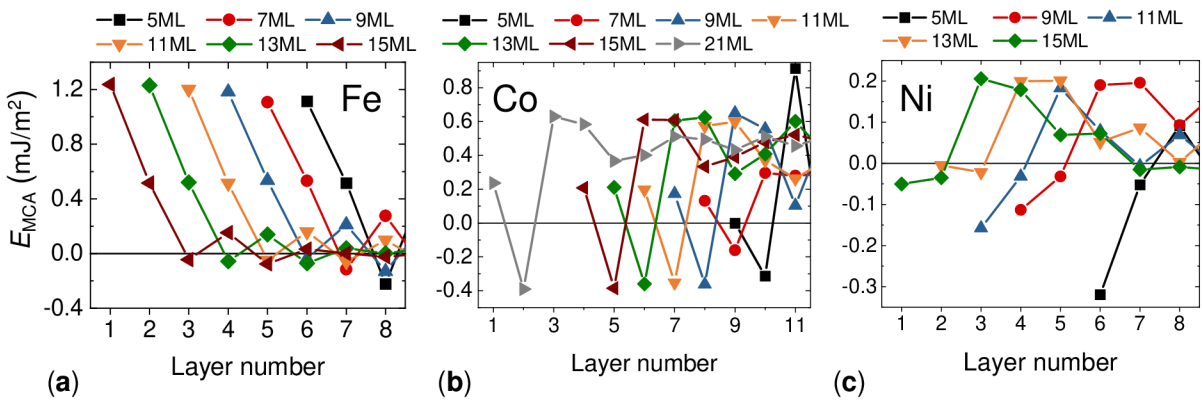

Figure A.1: Layer-resolved E_{MCA} for different thicknesses of (a) Fe, (b) Co, and (Ni) on MgO. © 2021 American Physical Society [120].

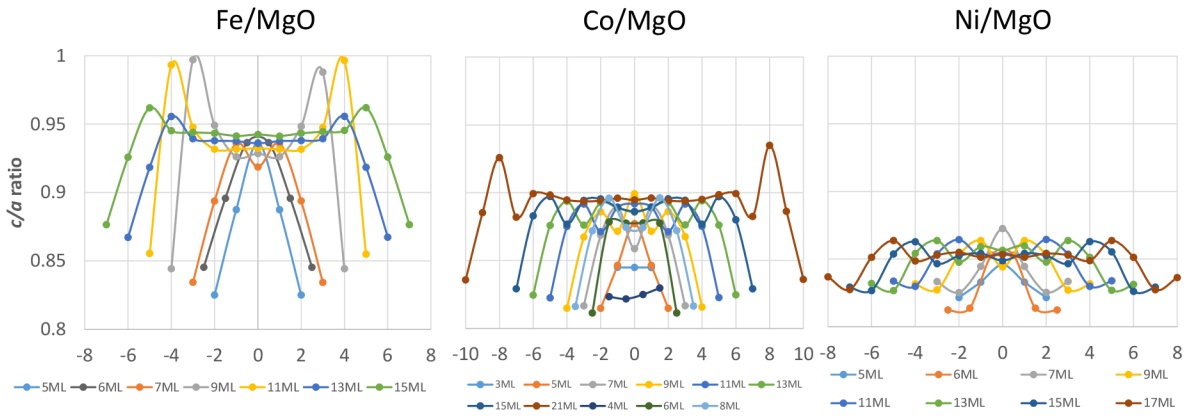

Figure A.2: Layer-resolved c/a ratios for different thicknesses of (a) Fe, (b) Co, and (Ni) on MgO. Across all the thicknesses for a given metal, the strain in the bulk-like layers (around layer 0) is similar.

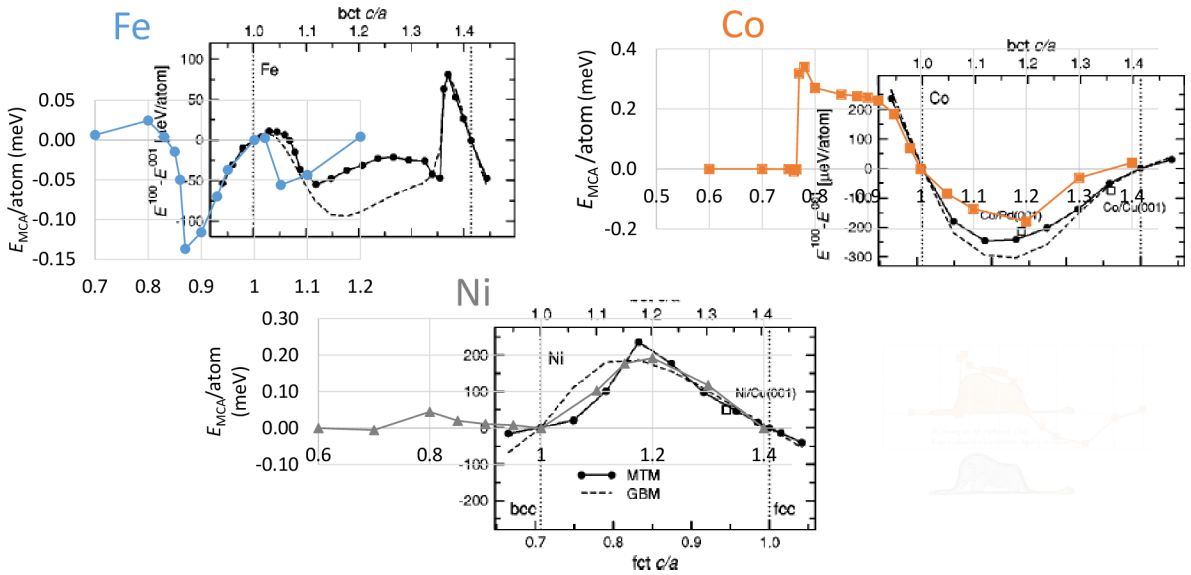

Figure A.3: Comparing the E_{MCA} vs. thickness plots from Sec. 3.6 with those of Burkert *et al.* [127], where they calculated only the region $c/a > 1$. The results agree reasonably well.